




# Fabricating 2D/2D/2D heterojunction of graphene oxide mediated g-C<sub>3</sub>N<sub>4</sub> and ZnV<sub>2</sub>O<sub>6</sub> composite with kinetic modelling for photocatalytic CO<sub>2</sub> reduction to fuels under UV and visible light

Abdullah Bafaqeer<sup>1,3</sup>, Muhammad Tahir<sup>1,\*</sup> , Nor Aishah Saidina Amin<sup>1</sup>, Abdul Rahman Mohamed<sup>2</sup>, and Mohd Azizi Che Yunus<sup>1</sup>

<sup>1</sup>School of Chemical and Energy Engineering, Universiti Teknologi Malaysia, UTM, 81310 Johor Bahru, Johor, Malaysia

<sup>2</sup>School of Chemical Engineering, Universiti Sains Malaysia, Penang, Malaysia

<sup>3</sup>Faculty of Chemical Engineering, Hadhramout University, Al-Mukalla, Hadhramout, Yemen

**Received:** 6 October 2020

**Accepted:** 4 February 2021

**Published online:**

24 February 2021

© The Author(s), under exclusive licence to Springer Science+Business Media, LLC part of Springer Nature 2021

## ABSTRACT

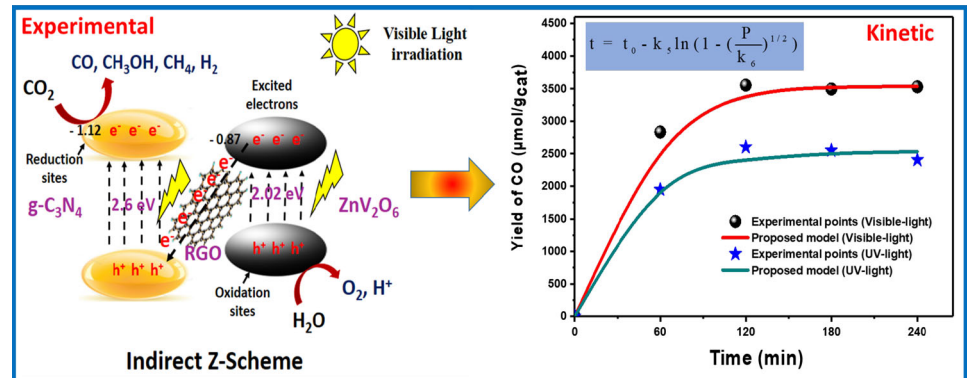
Two dimensional (2D) reduced-graphene-oxide/g-C<sub>3</sub>N<sub>4</sub> modified 2D ZnV<sub>2</sub>O<sub>6</sub> heterojunction for enhanced photocatalytic CO<sub>2</sub> reduction has been investigated. The catalysts were fabricated using one-pot solvothermal method and were tested in a fixed-bed reactor under visible and UV-light. The ZnV<sub>2</sub>O<sub>6</sub>/RGO/g-C<sub>3</sub>N<sub>4</sub> composite catalyst demonstrated excellent photoactivity for CO<sub>2</sub> reduction to CO and hydrocarbons under visible light. The maximum CO yield rate of 2802.9 μmol g<sup>-1</sup> h<sup>-1</sup> was obtained over the composite, which is 7.4 and 1.7 times higher than using g-C<sub>3</sub>N<sub>4</sub> and ZnV<sub>2</sub>O<sub>6</sub>, respectively. The improved activity attributing to synergistic effect of 2D layer heterojunction with enhanced charges separation by RGO mediator under visible light. Comparatively, 2 times lower productivity was obtained under UV-light than visible-light due to higher visible-light absorption. The time-dependent kinetic-model was further developed to understand the influence of photocatalytic oxidation and reduction processes on the reaction chemistry. The model is based on Langmuir–Hinshelwood (L–H) mechanism to understand the formation rates of products during photocatalytic CO<sub>2</sub> conversion with water vapours. Kinetic reveals surface reaction is a rate limiting step, which depends on the generation of charge carrier with higher light absorption. The findings from the experimental and kinetic-model would be useful to understand photo-catalytic reaction engineering in solar energy applications.

Handling Editor: Dale Huber.

Address correspondence to E-mail: m.tahir@utm.my

<https://doi.org/10.1007/s10853-021-05906-1>

## GRAPHICAL ABSTRACT



## Introduction

During the last years, the rapid increment of atmospheric carbon dioxide (CO<sub>2</sub>) concentration has attracted considerable attention due to its great effect on the global climate. Furthermore, the rapid depletion of fossil resources is leading to the urgent need for the development of alternative energy sources [1, 2]. As a renewable, safe, and economic technique, the photo-reduction of CO<sub>2</sub> to valuable fuels using clean solar energy has become a most promising strategy to simultaneously resolve the two aforementioned problems [3–6]. Since the pioneering work of Inoue and colleagues [7], photocatalytic CO<sub>2</sub> reduction has been extensively studied and a number of photo-catalysts have been developed such as TiO<sub>2</sub> [8, 9], ZnO [10], AgBr [11] and MoO<sub>2</sub> [12]. However, these semiconductors exhibit low photocatalytic activity because of rapid electron–hole pair recombination [13, 14]. Therefore, highly efficient and stable photo-catalysts for CO<sub>2</sub> reduction, especially functional under solar light irradiation, would be promising for sustainable solar fuels production.

Recently, 2D layered graphitic carbon nitride (g-C<sub>3</sub>N<sub>4</sub>), a visible light-responsive polymer, has attracted substantial attention due to high photostability, appropriate band structure, ease of preparation, low cost and nontoxicity [15–17]. However, CO<sub>2</sub> reduction rate of g-C<sub>3</sub>N<sub>4</sub> is lower because of high recombination rate of charge carrier [18, 19]. The

photocatalytic performance of g-C<sub>3</sub>N<sub>4</sub> can be enhanced through several methods which include metals and non-metals loading, surface modification and coupling with other semiconductors [20]. The proficiency of g-C<sub>3</sub>N<sub>4</sub> can be significantly enhanced by coupling it with a second semiconductor to construct a heterojunction among the semiconductors. The formation of heterojunction is very promising to maximize photocatalytic activity as it would be beneficial to adjust the band positions with proficient charge carrier separation [21–23]. In this perspective several research efforts were made to improve g-C<sub>3</sub>N<sub>4</sub> efficiency for effective CO<sub>2</sub> photo-reduction to fuels, for example., g-C<sub>3</sub>N<sub>4</sub>/ZnO [24], g-C<sub>3</sub>N<sub>4</sub>/WO<sub>3</sub> [25], MnO<sub>2</sub>/g-C<sub>3</sub>N<sub>4</sub> [26], g-C<sub>3</sub>N<sub>4</sub>/NiAl-LDH [27] and g-C<sub>3</sub>N<sub>4</sub>/SnS<sub>2</sub> [28]. Recently, ZnV<sub>2</sub>O<sub>6</sub>/g-C<sub>3</sub>N<sub>4</sub> nanosheets heterojunction with 2D/2D structure has been reported with enhanced photoactivity and productivity [29]. Under visible light, 2D/2D interface hetero-junction exhibited enhanced photocatalytic CO<sub>2</sub> conversion to methanol (CH<sub>3</sub>OH) and CO, whereas the performance was much higher than using pristine g-C<sub>3</sub>N<sub>4</sub> and ZnV<sub>2</sub>O<sub>6</sub> samples. However, for binary composites, there is limitations in charge carrier transportation and separation, which can be boosted by introducing a mediator among the semiconductors. Therefore, a ternary nanocomposite system by introducing co-photocatalyst that can deliver the effective redox reaction sites, lower the reaction activation energy and inhibit the possible charge recombination.

Reduced graphene oxide (RGO) is a well-known co-catalyst due to its large surface area, superior electron mobility, high transparency and two-dimensional (2D) layered structure [30]. There has been growing interest on the utilization of RGO as a mediator to improve photocatalytic activities with faster charge transfer rates such as BiOBr/reduced graphene oxide/g-C<sub>3</sub>N<sub>4</sub> [31], Bi<sub>2</sub>WO<sub>6</sub>/reduced graphene oxide/g-C<sub>3</sub>N<sub>4</sub> [32], Cd<sub>0.5</sub>Zn<sub>0.5</sub>S/reduced graphene oxide/g-C<sub>3</sub>N<sub>4</sub> [33], g-C<sub>3</sub>N<sub>4</sub>/reduced graphene oxide/BiVO<sub>4</sub> [21] and g-C<sub>3</sub>N<sub>4</sub>/reduced graphene oxide /FeWO<sub>4</sub> [34] ternary composite samples. Therefore, combining reduced graphene oxide with ZnV<sub>2</sub>O<sub>6</sub>/g-C<sub>3</sub>N<sub>4</sub> would be beneficial to construct a ternary nanocomposite which would provide excellent redox potential for photoreduction of CO<sub>2</sub> to fuels under solar-light illuminations.

Herein, self-assembly fabrication of reduced graphene oxide/g-C<sub>3</sub>N<sub>4</sub> modified ZnV<sub>2</sub>O<sub>6</sub> nanocomposite for dynamic photocatalytic CO<sub>2</sub> conversion to fuels has been investigated. The efficiency of nanocomposite photocatalysts was investigated utilizing visible and UV light illuminations in a fixed-bed photoreactor. The ternary nanocomposite of reduced graphene oxide/g-C<sub>3</sub>N<sub>4</sub> modified ZnV<sub>2</sub>O<sub>6</sub> exhibited improved photocatalytic performance for converting CO<sub>2</sub> to CO, CH<sub>3</sub>OH, CH<sub>4</sub> and H<sub>2</sub> under visible-light illuminations. The reaction mechanism for the conversion of CO<sub>2</sub> with H<sub>2</sub>O over the ternary RGO/g-C<sub>3</sub>N<sub>4</sub> coupled ZnV<sub>2</sub>O<sub>6</sub> nanocomposite has been proposed to further understand the role of each component in stimulating photocatalytic activity. Finally, the L–H approach based kinetic model is developed to determine the kinetic rate in a heterogeneous photocatalytic system under solar energy.

## Experimental

### Materials

Ammonia (NH<sub>3</sub>) solution and ammonium metavanadate (NH<sub>4</sub>VO<sub>3</sub>) were purchased from Merck, Germany. Zinc acetate (Zn(O<sub>2</sub>CCH<sub>3</sub>)<sub>2</sub>), melamine (99.0%), nitric acid, zinc oxide and N,N-dimethyl formamide (DMF) were supplied by Sigma-Aldrich.

### Synthesis of g-C<sub>3</sub>N<sub>4</sub> nanosheets

The bulk g-C<sub>3</sub>N<sub>4</sub> was prepared via thermal treatment of melamine using alumina crucible. In a typical synthesis process, 4 g melamine (Sigma Aldrich AR ≥ 99%) was placed in a crucible and heated to 550 °C for 2 h in a furnace under air atmosphere. The g-C<sub>3</sub>N<sub>4</sub> obtained was ground to obtain fine powder and was utilized for the surface charge modification by functionalization with nitric acid solution. In detail, 2 g of g-C<sub>3</sub>N<sub>4</sub> powder was immersed in a nitric acid solution (0.1 M HNO<sub>3</sub>) by stirring for 4 h. The mixture was washed with distilled water to remove any residual alkaline species (e.g., ammonia). After this, it was dried at 80 °C for 12 h and was ground to get yellow colour powder named as 2D g-C<sub>3</sub>N<sub>4</sub> nanosheets.

### Preparation of reduced graphene oxide/g-C<sub>3</sub>N<sub>4</sub> modified ZnV<sub>2</sub>O<sub>6</sub> nanocomposite

ZnV<sub>2</sub>O<sub>6</sub> nanosheets were fabricated by a one-pot solvothermal approach as reported previously [35]. In brief, 2.052 mmol of NH<sub>4</sub>VO<sub>3</sub> was immersed in a 25 ml DMF by stirring for 10 min (mixture A). Subsequently, Zn(O<sub>2</sub>CCH<sub>3</sub>)<sub>2</sub> was added to mixture A and stirred until a uniform suspension was obtained (mixture B). Then, H<sub>2</sub>C<sub>2</sub>O<sub>4</sub>·2H<sub>2</sub>O (oxalic acid) was added in mixture B of NH<sub>4</sub>VO<sub>3</sub> at 1:3 (oxalic acid/NH<sub>4</sub>VO<sub>3</sub>) ratio (mixture C). In parallel, 4 wt% of graphene (GO) was immersed in 25 ml DMF by stirring for 10 min. Also, 100 wt% of g-C<sub>3</sub>N<sub>4</sub> (ZnV<sub>2</sub>O<sub>6</sub>/g-C<sub>3</sub>N<sub>4</sub> ratio of 1.0) and 25 ml of DMF were mixed to generate a graphitic carbon nitride suspension. After that, g-C<sub>3</sub>N<sub>4</sub> and reduced graphene oxide suspensions were added to the mixture C and stirred for 30 min (mixture D). The suspension mixture D was then transferred to a Teflon lined stainless-steel autoclave (100 mL) and heated at 200 °C for 24 h. The resultant product was washed repeatedly with absolute ethanol and dried at 80 °C for 12 h to obtain the reduced graphene oxide/g-C<sub>3</sub>N<sub>4</sub> modified ZnV<sub>2</sub>O<sub>6</sub> nanocomposite. The composite obtained has ZnV<sub>2</sub>O<sub>6</sub>/g-C<sub>3</sub>N<sub>4</sub> ratio 1 with 4 wt% RGO loading and named as reduced graphene oxide mediated g-C<sub>3</sub>N<sub>4</sub> and ZnV<sub>2</sub>O<sub>6</sub> composite (ZnV<sub>2</sub>O<sub>6</sub>/RGO/g-C<sub>3</sub>N<sub>4</sub>). For comparison, ZnV<sub>2</sub>O<sub>6</sub>/reduced graphene oxide (4 wt%) and ZnV<sub>2</sub>O<sub>6</sub>/g-C<sub>3</sub>N<sub>4</sub> (100 wt%) samples were also prepared using the same process. The schematics for the preparation of reduced graphene

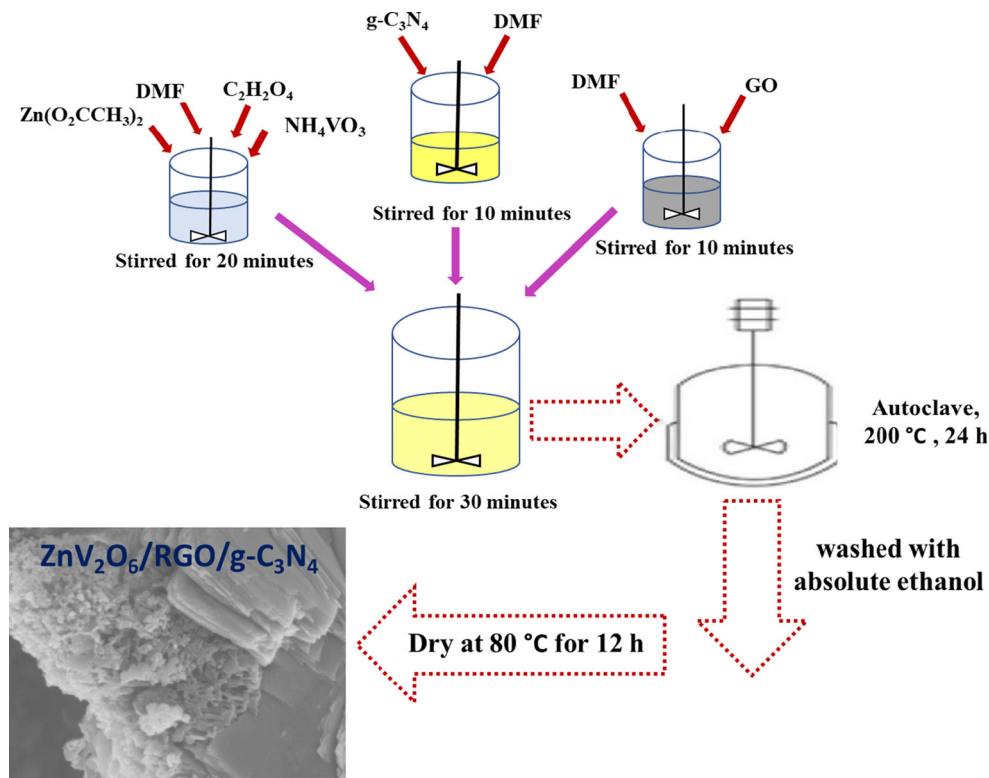


**Figure 1** Schematics illustration for the synthesis of  $\text{ZnV}_2\text{O}_6/\text{RGO}/\text{g-C}_3\text{N}_4$  heterojunction.

oxide/ $\text{g-C}_3\text{N}_4$  modified  $\text{ZnV}_2\text{O}_6$  nanocomposite has been demonstrated in Fig. 1.

### Characterizations of photocatalyst

X-ray diffraction (XRD) of the photocatalysts were recorded via Bruker diffractometer system (40 kV,  $\lambda = 0.154178$  nm) with Cu  $\text{K}\alpha$  as a radiation source. The XPS (X-ray Photoelectron Spectroscopy) measurements were conducted using Ultra DLD Shimadzu machine. The TEM images were obtained using HITACHI-HT7700 equipment. The corresponding elemental mapping images and field emission scanning electron microscopy (FESEM) were obtained by a Zeiss Crossbeam 340 system. PL spectra of the photocatalysts were determined by Raman Spectrophotometer (HORIBA Scientific). The surface areas of the photocatalysts were investigated utilizing Brunauer–Emmett–Teller (BET) method with Micrometric ASAP 2020 analyser. UV–Vis DR (diffuse reflectance) spectra were attained utilizing Agilent, Cary 100 spectrophotometer (Model G9821A) equipped with integrated sphere.

### Photoactivity measurement

Photocatalytic  $\text{CO}_2$  reduction with  $\text{H}_2\text{O}$  system was carried out in a stainless steel photoreactor as reported in our previous work [29]. The light source utilized to activate the photoreactions was a 200 W Hg lamp with a light intensity  $150 \text{ mW}/\text{cm}^2$  for UV illumination source. The photoactivity was further investigated utilizing a solar simulator lamp with a light intensity  $100 \text{ mW}/\text{cm}^2$ . The both the lamps were positioned at the top of the photoreactor and cooling fans were provided to remove the lamp heat. Typically, 100 mg powder photocatalyst was evenly distributed at the bottom of the cylindrical stainless-steel chamber. High purity  $\text{CO}_2$  (purity = 99.99%), regulated by mass flow controller with a total flow rate  $5 \text{ mL}/\text{min}$ , was bubbled through water saturator to carry moisture. The feed mixture ( $\text{CO}_2$ ,  $\text{H}_2\text{O}$ ) was passed through the reactor for 30 min to remove air and to saturate the catalyst with the reactants. The water saturator temperature was adjusted to  $30 \text{ }^\circ\text{C}$  in all the experiments. All the experiments were conducted in a continuous flow system without providing external heat source. The gaseous products were analysed utilizing online system of gas

chromatograph (GC Agilent 6890 N, USA) equipped with TCD and FID detectors. The TCD detector was employed for the analysis of CO, CO<sub>2</sub> and H<sub>2</sub>, whereas, FID detector was helpful to analyse methanol and hydrocarbons.

### Langmuir–hinshelwood (L–H) kinetic model

In heterogeneous photocatalysis, surface reaction rates are supposed to depend on the fraction of active sites covered by different species. In an irreversible bimolecular reaction, the rate of reaction of molecules that are competitively adsorbed on the same type of active sites depends on the probability of the attachment of molecules to the adjacent sites. Furthermore, adsorption occurs over the catalyst surface, when a molecule with sufficient energy strikes over the vacant sites or unoccupied sites of the surface [36, 37]. The procedure is described as the reaction between a molecule from the gas phase (either CO<sub>2</sub> or H<sub>2</sub>O) and un-occupied site ‘S’. When there is competitive adsorption between H<sub>2</sub>O and CO<sub>2</sub>, then adsorption and desorption reactions for H<sub>2</sub>O and CO<sub>2</sub> molecules are illustrated by Eqs. (1–4).

$$r_{ads,CO_2} = k_{1,CO_2}P_{CO_2}(1 - \theta_{CO_2} - \theta_{H_2O}) \tag{1}$$

$$r_{ads,CO_2} = k_{2,CO_2}\theta_{CO_2} \tag{2}$$

$$r_{ads,H_2O} = k_{1,H_2O}P_{H_2O}(1 - \theta_{CO_2} - \theta_{H_2O}) \tag{3}$$

$$r_{ads,H_2O} = k_{2,H_2O}\theta_{H_2O} \tag{4}$$

After correlating Eqs. (1–4), the final equations for the competition adsorption are demonstrated by reaction in Eqs. (5) and (6).

$$\theta_{CO_2} = \frac{K_{CO_2}P_{CO_2}}{1 + K_{CO_2}P_{CO_2} + K_{H_2O}P_{H_2O}} \tag{5}$$

$$\theta_{H_2O} = \frac{K_{H_2O}P_{H_2O}}{1 + K_{CO_2}P_{CO_2} + K_{H_2O}P_{H_2O}} \tag{6}$$

The Langmuir–Hinshelwood (L–H) mechanism can be used to isotherm kinetic model using assumption that reactants and products are adsorbed on different catalysts active sites. The rate of reaction can be explained using L–H model as described in Eqs. (7) and (8) [38].

$$r_s = kI^a\theta_{CO_2}\theta_{H_2O} \tag{7}$$

$$r_s = k_1I^a \frac{K_{CO_2}P_{CO_2}K_{H_2O}P_{H_2O}}{N} \tag{8}$$

where,

$$N = (K_{CO_2}P_{CO_2} + K_{H_2O}P_{H_2O} + K_{CH_4}P_{CH_4} + K_{CO}P_{CO} + K_{O_2}P_{O_2})^2$$

where, *r<sub>s</sub>* is the rate of surface reaction, *k<sub>1</sub>* is the rate constants and *K<sub>CO<sub>2</sub></sub>*, *K<sub>H<sub>2</sub>O</sub>*, *K<sub>CH<sub>4</sub></sub>*, *K<sub>CO</sub>* and *K<sub>O<sub>2</sub></sub>* are the ratios of adsorption to desorption equilibrium rate constants for CO<sub>2</sub>, H<sub>2</sub>O, CH<sub>4</sub>, O<sub>2</sub> and CO, respectively. *I* is the UV light or visible light flux intensity for which kinetic constants is evaluated and “*a*” is the reaction order of light intensity. Throughout photocatalytic conversion of CO<sub>2</sub> over the surface of photocatalyst, the rate equation can be obtained with the assumptions. Therefore, L–H model is an attractive approach to determine reaction rate constant and activation energy of different heterogeneous systems.

## Results and discussion

### Characterization of photo-catalysts

The X-ray diffraction (XRD) patterns of the ZnV<sub>2</sub>O<sub>6</sub> nanosheets and ZnV<sub>2</sub>O<sub>6</sub> calcined were reported previously [29]. The ZnV<sub>2</sub>O<sub>6</sub> showed several peaks at 2θ of 14.27°, 22.59°, 26.27°, 31.28°, 35.55° and 47.60°, which are characteristics of zinc vanadium oxide. Besides, the XRD pattern of the ZnV<sub>2</sub>O<sub>6</sub> shows pronounced diffraction peak located at around 2θ = 10.0° belonging to metal alkoxide, due to using as prepared samples without calcination at higher temperature [39, 40]. The XRD patterns of reduced graphene oxide, g-C<sub>3</sub>N<sub>4</sub>, ZnV<sub>2</sub>O<sub>6</sub>, ZnV<sub>2</sub>O<sub>6</sub>/g-C<sub>3</sub>N<sub>4</sub> and reduced graphene oxide/g-C<sub>3</sub>N<sub>4</sub> modified ZnV<sub>2</sub>O<sub>6</sub> photocatalysts are displayed in Fig. 2. The reduced graphene oxide shows two peaks at 2θ of 23.67° and 42.83°, which can be assigned to the (002) and (200) plane of reduced graphene oxide material [41]. For the bulk g-C<sub>3</sub>N<sub>4</sub>, two distinct peaks were discovered at appropriately 2θ of 27.52° and 12.96°. The strong peak at 2θ = 27.53° was index to the (002) plane, another weak peak at 12.96° can be attributed to the (100) plane [42, 43]. Both ZnV<sub>2</sub>O<sub>6</sub> and g-C<sub>3</sub>N<sub>4</sub> phases are observed in the ZnV<sub>2</sub>O<sub>6</sub>/g-C<sub>3</sub>N<sub>4</sub> nanocomposite. However, peak of reduced graphene oxide was not appeared in the reduced graphene oxide/g-C<sub>3</sub>N<sub>4</sub> modified ZnV<sub>2</sub>O<sub>6</sub> nanocomposite. This

**Figure 2** XRD pattern of RGO, g-C<sub>3</sub>N<sub>4</sub>, ZnV<sub>2</sub>O<sub>6</sub>, ZnV<sub>2</sub>O<sub>6</sub>/g-C<sub>3</sub>N<sub>4</sub> and ZnV<sub>2</sub>O<sub>6</sub>/RGO/g-C<sub>3</sub>N<sub>4</sub> samples.

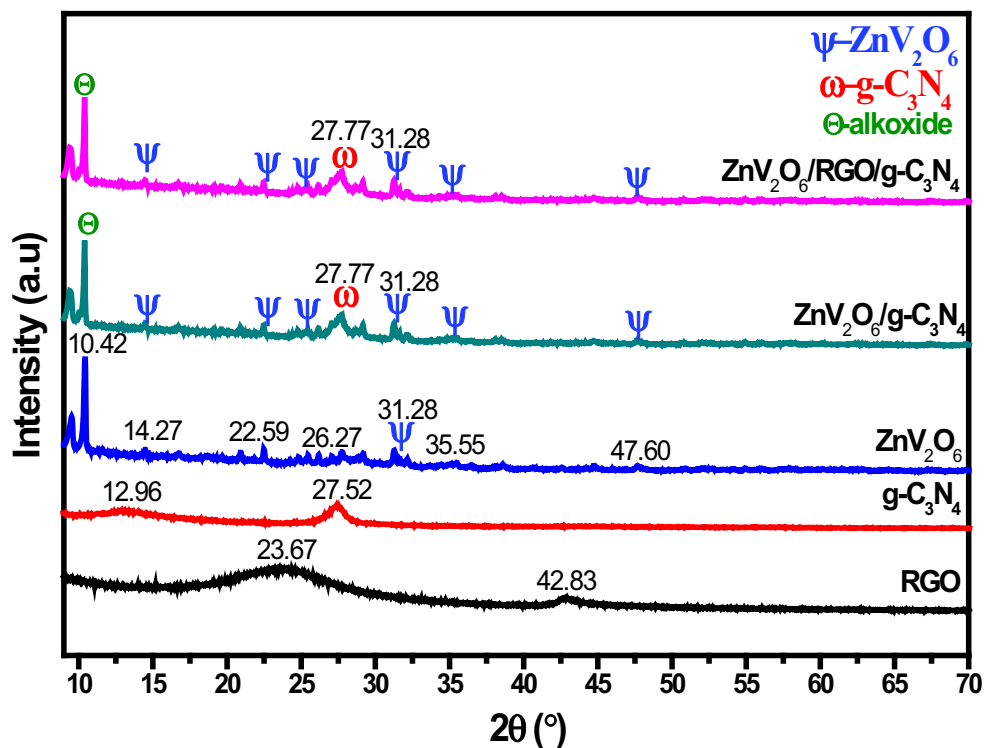


**Table 1** Summary of BET and BJH surface area of ZnV<sub>2</sub>O<sub>6</sub>, g-C<sub>3</sub>N<sub>4</sub> and RGO modified composite photocatalysts

Sample	S <sub>BET</sub> (m <sup>2</sup> /g)	S <sub>BJH</sub> (m <sup>2</sup> /g)	E <sub>bg</sub> (eV)
ZnV <sub>2</sub> O <sub>6</sub>	11.6	3.8	2.02
g-C <sub>3</sub> N <sub>4</sub>	11.0	11.6	2.60
ZnV <sub>2</sub> O <sub>6</sub> /g-C <sub>3</sub> N <sub>4</sub>	11.3	4.8	2.21
ZnV <sub>2</sub> O <sub>6</sub> /RGO/g-C <sub>3</sub> N <sub>4</sub>	12.2	8.9	2.16

was obviously due to its low content (4 wt%) and possibly below the detection limit of XRD machine as similarly reported previously [2].

The S<sub>BET</sub> (BET surface area) and S<sub>BJH</sub> (BJH surface area) of all the samples were calculated using N<sub>2</sub> adsorption–desorption isotherms and results are presented in Table 1. The S<sub>BET</sub> of 11.6, 11.0 and 11.3 m<sup>2</sup>/g were obtained for ZnV<sub>2</sub>O<sub>6</sub>, g-C<sub>3</sub>N<sub>4</sub> and ZnV<sub>2</sub>O<sub>6</sub>/g-C<sub>3</sub>N<sub>4</sub> heterojunction, respectively. This reveals that both g-C<sub>3</sub>N<sub>4</sub> and ZnV<sub>2</sub>O<sub>6</sub> have similar BET surface areas, and there was no effect on altering the surface area in constructing their heterojunction. Similarly, a BET surface area of 12.2 m<sup>2</sup>/g was obtained when reduced graphene oxide was coupled with g-C<sub>3</sub>N<sub>4</sub>/ZnV<sub>2</sub>O<sub>6</sub> composite, confirming no

effect on BET surface area. Comparatively, g-C<sub>3</sub>N<sub>4</sub> has higher S<sub>BJH</sub> surface area (11.0 m<sup>2</sup>/g) than ZnV<sub>2</sub>O<sub>6</sub> (3.8 m<sup>2</sup>/g), which was reduced to 4.8 m<sup>2</sup>/g in ZnV<sub>2</sub>O<sub>6</sub>/g-C<sub>3</sub>N<sub>4</sub> composite. In addition, when RGO was loaded with ZnV<sub>2</sub>O<sub>6</sub>/g-C<sub>3</sub>N<sub>4</sub>, a BJH surface area of 8.9 m<sup>2</sup>/g was obtained, but it was lower than pristine g-C<sub>3</sub>N<sub>4</sub>. This reveals that composite samples have not much higher surface area than pristine g-C<sub>3</sub>N<sub>4</sub> and ZnV<sub>2</sub>O<sub>6</sub>, thus any photoactivity enhancement would be due to charge carrier separation with the involvement of higher light absorption.

The morphology of photocatalysts was investigated utilizing FESEM as presented in Fig. 3. Figure 3a presents FE-SEM image of ZnV<sub>2</sub>O<sub>6</sub> containing large number of sheets with 2D structures. The EDX mapping analysis in Fig. 3b reveals the distribution of Zn, V, C and O elements over ZnV<sub>2</sub>O<sub>6</sub> sample, whereas, EDX spectra of elements in Fig. 3c confirms the presence of zinc, vanadium, oxygen and carbon elements in ZnV<sub>2</sub>O<sub>6</sub> sample. As depicted in Fig. 3d, the g-C<sub>3</sub>N<sub>4</sub> presented a 2D morphology, a layered, flat, sheet-like structure having hollows and a lamellar structure. Figure 3e displays EDX mapping analysis of g-C<sub>3</sub>N<sub>4</sub>/ZnV<sub>2</sub>O<sub>6</sub> composite. It could be seen, all the elements (Zn, V, C, N, and O) are uniformly distributed over the composite 2D layered structure. The existence of all the elements in

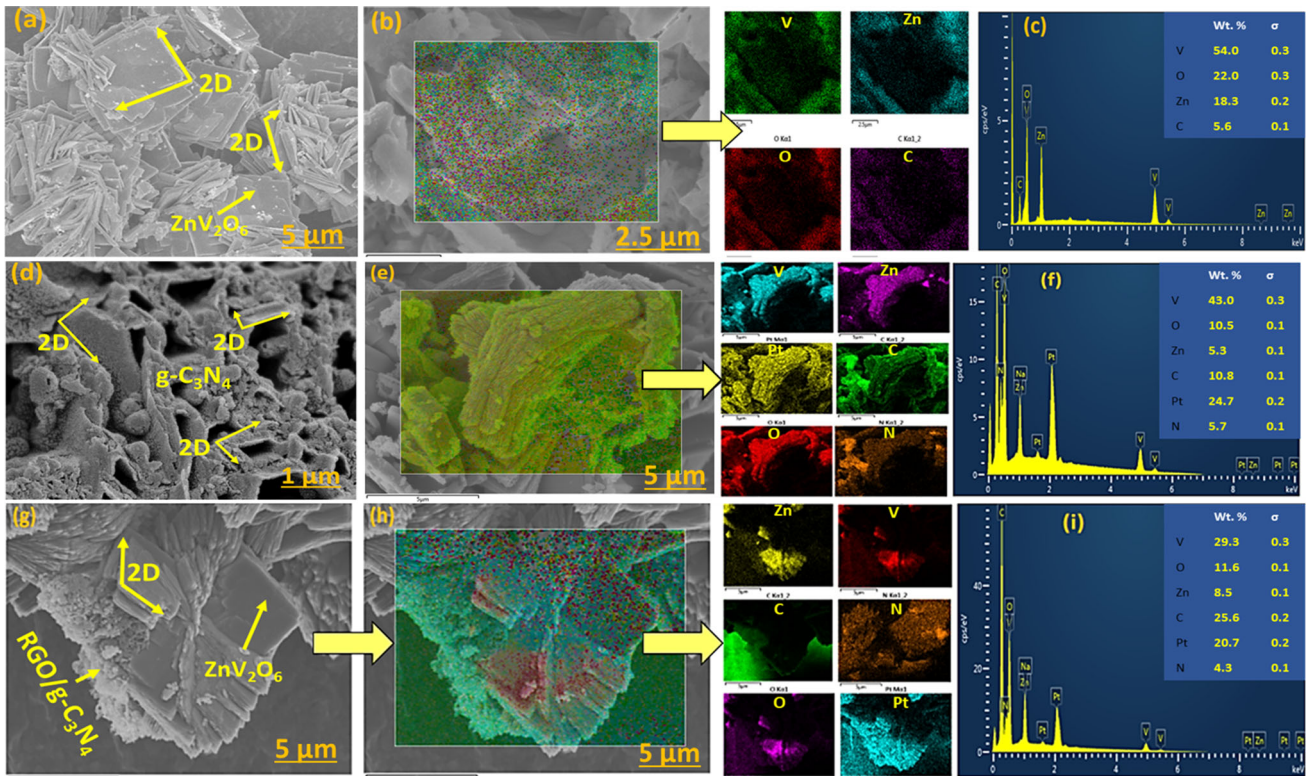


**Figure 3** FESEM micrographs of **a**  $\text{ZnV}_2\text{O}_6$  nanosheets; **b, c** EDX mapping of  $\text{ZnV}_2\text{O}_6$ ; **d**  $\text{ZnV}_2\text{O}_6/\text{g-C}_3\text{N}_4$  nanosheets; **e, f** EDX mapping of  $\text{ZnV}_2\text{O}_6/\text{g-C}_3\text{N}_4$ ; **g**  $\text{ZnV}_2\text{O}_6/\text{RGO}/\text{g-C}_3\text{N}_4$  composite; **h, i** EDX mapping of  $\text{ZnV}_2\text{O}_6/\text{RGO}/\text{g-C}_3\text{N}_4$ .

$\text{ZnV}_2\text{O}_6/\text{g-C}_3\text{N}_4$  composite were further confirmed using EDX spectra as demonstrated in Fig. 3f. Obviously, the existence of zinc, vanadium, oxygen, carbon and nitrogen in  $\text{ZnV}_2\text{O}_6/\text{g-C}_3\text{N}_4$  nanocomposite could be seen from the obvious spectra peaks. Figure 3g presents FESEM image of the reduced graphene oxide coupled  $\text{g-C}_3\text{N}_4/\text{ZnV}_2\text{O}_6$  nanocomposite. Evidently, a good interaction among all the components could be seen in RGO mediated  $\text{g-C}_3\text{N}_4/\text{ZnV}_2\text{O}_6$  ternary composite. From this point of view, it is confirmed the Z-scheme heterojunction. The EDX mapping analysis in Fig. 3 h further confirms uniform distribution of all the elements over the composite catalyst surface. The presence of all the elements such as vanadium, zinc, carbon, nitrogen and oxygen were further identified from EDX spectra as demonstrated in Fig. 3i. The presence of platinum (Pt) was due to samples coated with Pt before analysis.

The morphology and the microstructure of the  $\text{ZnV}_2\text{O}_6$ , reduced graphene oxide,  $\text{g-C}_3\text{N}_4$  and reduced graphene oxide/ $\text{g-C}_3\text{N}_4$  modified  $\text{ZnV}_2\text{O}_6$  photocatalysts were further investigated using HRTEM as presented in Fig. 4. The  $\text{ZnV}_2\text{O}_6$  consists

of plentiful nanosheets with 2D structure as exhibited in Fig. 4a. Figure 4b shows 2D nanostructure of reduced graphene oxide with obvious wrinkles and folds. The  $\text{g-C}_3\text{N}_4$  exhibits a thin layered structure with a 2D morphology as displayed in Fig. 4c. As exhibited in Fig. 4d and e, the HRTEM image clarifies that the reduced graphene oxide and  $\text{g-C}_3\text{N}_4$  are effectively deposited on the surface of  $\text{ZnV}_2\text{O}_6$  nanosheets. It can be also seen that the RGO mediated  $\text{ZnV}_2\text{O}_6/\text{g-C}_3\text{N}_4$ , which confirmed heterojunction formation of  $\text{ZnV}_2\text{O}_6/\text{RGO}/\text{g-C}_3\text{N}_4$  photocatalysts. The marked lattice spaces of 0.48 nm are in good agreement with the (111) plane of  $\text{ZnV}_2\text{O}_6$  nanosheets. The lattices fringes of  $\text{g-C}_3\text{N}_4$  in the reduced graphene oxide/ $\text{g-C}_3\text{N}_4$  modified  $\text{ZnV}_2\text{O}_6$  nanocomposite is about 0.32 nm, corresponding to (002) plane [44]. The SAED pattern of reduced graphene oxide/ $\text{g-C}_3\text{N}_4$  modified  $\text{ZnV}_2\text{O}_6$  nanocomposite in Fig. 4f presents an obvious crystalline ring due to considerable crystallization of  $\text{ZnV}_2\text{O}_6$ .

To examine chemical states of the elements in the  $\text{ZnV}_2\text{O}_6/\text{g-C}_3\text{N}_4$  and reduced graphene oxide/ $\text{g-C}_3\text{N}_4$  modified  $\text{ZnV}_2\text{O}_6$  photocatalysts, XPS measurements were conducted and results are

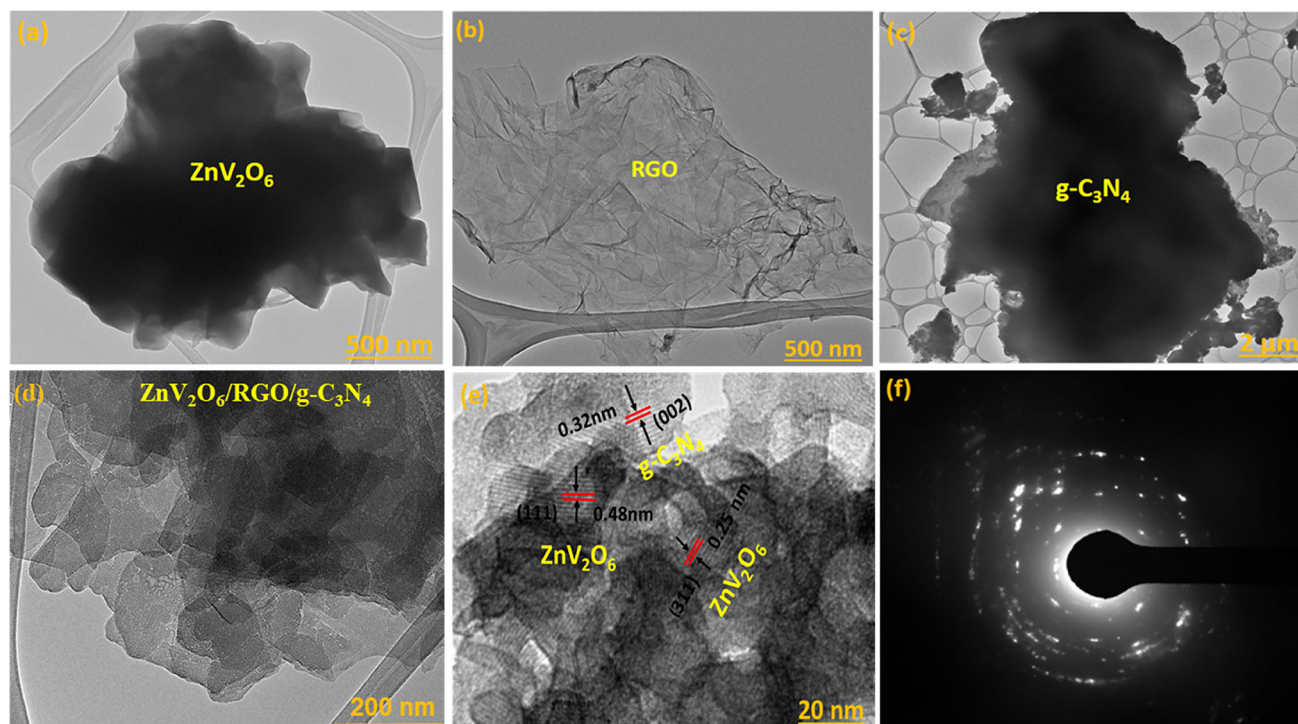


**Figure 4** TEM images of **a** ZnV<sub>2</sub>O<sub>6</sub>; **b** RGO; **c** g-C<sub>3</sub>N<sub>4</sub>; **d** ZnV<sub>2</sub>O<sub>6</sub>/RGO/g-C<sub>3</sub>N<sub>4</sub> sample; **e** d-spacing of ZnV<sub>2</sub>O<sub>6</sub>/RGO/g-C<sub>3</sub>N<sub>4</sub> sample; **f** SAED pattern of the ZnV<sub>2</sub>O<sub>6</sub>/RGO/g-C<sub>3</sub>N<sub>4</sub> sample.

demonstrated in Fig. 5. The XPS survey spectra in Fig. 5a shows that the V, Zn, N, C and O elements were observed in the ZnV<sub>2</sub>O<sub>6</sub>/g-C<sub>3</sub>N<sub>4</sub> and reduced graphene oxide/g-C<sub>3</sub>N<sub>4</sub> modified ZnV<sub>2</sub>O<sub>6</sub> nanocomposite samples. Figure 5b displays high-resolution Zn 2p XPS spectra of ZnV<sub>2</sub>O<sub>6</sub>/g-C<sub>3</sub>N<sub>4</sub> and RGO mediated ZnV<sub>2</sub>O<sub>6</sub>/g-C<sub>3</sub>N<sub>4</sub> samples. The two obvious signals of Zn 2p at 1045.2 and 1022.3 eV were observed for ZnV<sub>2</sub>O<sub>6</sub>/g-C<sub>3</sub>N<sub>4</sub>, ascribes to Zn 2p<sub>1/2</sub> and Zn 2p<sub>3/2</sub>, respectively, confirming the presence of zinc as Zn<sup>+2</sup> state [45]. Similarly, Zn 2p peaks for reduced graphene oxide/g-C<sub>3</sub>N<sub>4</sub> modified ZnV<sub>2</sub>O<sub>6</sub> positioned at 1021.5 and 1044.6 eV, corresponds to Zn 2p<sub>1/2</sub> and Zn 2p<sub>3/2</sub>, respectively, belongs to zinc as Zn<sup>+2</sup> in the composite. Compared with ZnV<sub>2</sub>O<sub>6</sub>/g-C<sub>3</sub>N<sub>4</sub>, the peaks of Zn 2p<sub>1/2</sub> and Zn 2p<sub>3/2</sub> of Zn<sup>+2</sup> for reduced graphene oxide/g-C<sub>3</sub>N<sub>4</sub> modified ZnV<sub>2</sub>O<sub>6</sub> shifted towards lower binding energy. Figure 5c shows the high-resolution V 2p XPS spectrum of ZnV<sub>2</sub>O<sub>6</sub>/g-C<sub>3</sub>N<sub>4</sub> and RGO mediated ZnV<sub>2</sub>O<sub>6</sub>/g-C<sub>3</sub>N<sub>4</sub> samples. For ZnV<sub>2</sub>O<sub>6</sub>/g-C<sub>3</sub>N<sub>4</sub>, two signals at 524.8 and 517.4 eV are assigned to V 2p<sub>1/2</sub> and V 2p<sub>3/2</sub>, respectively, indicating the presence of vanadium as V<sup>+5</sup> [46]. Similarly, XPS peaks of V 2p in RGO/ZnV<sub>2</sub>O<sub>6</sub>/g-C<sub>3</sub>N<sub>4</sub> positioned at 516.9 and 524.3 eV for

V 2p<sub>1/2</sub> and V 2p<sub>3/2</sub>, respectively, confirming the presence of vanadium as V<sup>+5</sup>.

The high-resolution O 1s XPS spectra in Fig. 5d shows three peaks at 529.6, 531.7 and 534 eV for ZnV<sub>2</sub>O<sub>6</sub>/g-C<sub>3</sub>N<sub>4</sub> hetero-junction. The peaks positioned at 531.7 and 529.6 eV can be ascribed to the lattice oxygen in ZnV<sub>2</sub>O<sub>6</sub> sample, whereas the peak positioned at 534 eV is assigned to surface adsorbed oxygen types [39]. For reduced graphene oxide/g-C<sub>3</sub>N<sub>4</sub> modified ZnV<sub>2</sub>O<sub>6</sub> nanocomposite, the peaks are positioned at 529.9 and 531.4 eV. The former is attributed to the lattice oxygen and the latter is assigned to the adsorbed oxygen. The C 1s XPS spectrum of ZnV<sub>2</sub>O<sub>6</sub>/g-C<sub>3</sub>N<sub>4</sub> heterojunction and reduced graphene oxide/g-C<sub>3</sub>N<sub>4</sub> modified ZnV<sub>2</sub>O<sub>6</sub> nanocomposite are illustrated in Fig. 5e. For ZnV<sub>2</sub>O<sub>6</sub>/g-C<sub>3</sub>N<sub>4</sub> heterojunction, two obvious peaks in the range of 284–289 eV were fitted in the high resolution C 1s spectra, which is attributed to (C–O) and (C=O) type coordination in graphitic or amorphous carbons adsorbed on the surface [47]. The peak located at 290 eV detected in the spectra of ZnV<sub>2</sub>O<sub>6</sub>/g-C<sub>3</sub>N<sub>4</sub> heterojunction can be ascribed to sp<sup>2</sup> bonded C in the N–C–N coordination of g-C<sub>3</sub>N<sub>4</sub> [42]. For reduced graphene oxide/g-C<sub>3</sub>N<sub>4</sub> modified ZnV<sub>2</sub>O<sub>6</sub>



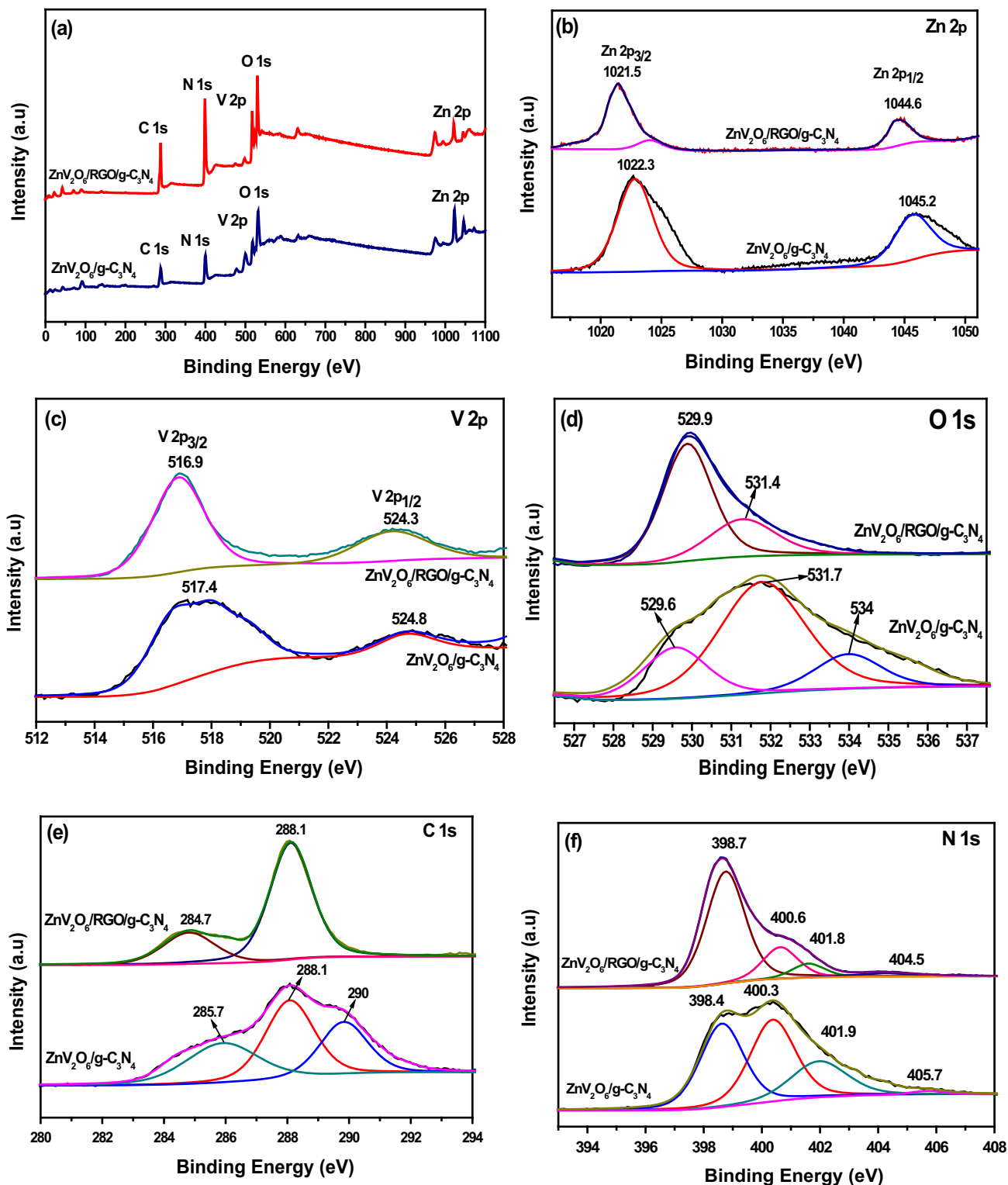


**Figure 5** a XPS survey spectra and high resolution XPS spectra of b Zn 2p; c V 2p; d O 1 s; e C 1 s and f N 1 s for the ZnV<sub>2</sub>O<sub>6</sub>/g-C<sub>3</sub>N<sub>4</sub> and ZnV<sub>2</sub>O<sub>6</sub>/RGO/g-C<sub>3</sub>N<sub>4</sub> composite.

nanocomposite, peaks appeared at 284.7 and 288.1 eV, corresponds to C–C and N–C–N,

respectively. Figure 5f shows the N 1 s XPS spectrum of ZnV<sub>2</sub>O<sub>6</sub>/g-C<sub>3</sub>N<sub>4</sub> and reduced graphene oxide/g-

C<sub>3</sub>N<sub>4</sub> modified ZnV<sub>2</sub>O<sub>6</sub> nanocomposite. The N 1 s XPS spectrum of ZnV<sub>2</sub>O<sub>6</sub>/g-C<sub>3</sub>N<sub>4</sub> nanocomposite shows four clear peaks at 404.5 eV (positive charge) [42], 401.9 eV (side N – H groups), 400.3 eV (ternary N groups, N-(C)<sub>3</sub>) and 398.4 eV (sp<sup>2</sup>-bonded N atoms, C – N = C) [48, 49]. Compared with ZnV<sub>2</sub>O<sub>6</sub>/g-C<sub>3</sub>N<sub>4</sub>, N 1 s peaks for reduced graphene oxide/g-C<sub>3</sub>N<sub>4</sub> modified ZnV<sub>2</sub>O<sub>6</sub> nanocomposite have a slight shift.

As discussed above, peaks of Zn, V and N has been shifted towards lower values when ZnV<sub>2</sub>O<sub>6</sub>/g-C<sub>3</sub>N<sub>4</sub> was coupled with RGO. This shift in peaks of in ternary composite towards lower binding energies would probably be due to distortion of band position during growth process in the presence of RGO. This suggests an intimate contact among the composite catalysts, thus would be favourable for promoting charge carrier separation [16]. However, all above discussion confirms the presence of pure RGO, g-C<sub>3</sub>N<sub>4</sub> and ZnV<sub>2</sub>O<sub>6</sub> in a binary ZnV<sub>2</sub>O<sub>6</sub>/g-C<sub>3</sub>N<sub>4</sub> and ternary RGO-ZnV<sub>2</sub>O<sub>6</sub>/g-C<sub>3</sub>N<sub>4</sub> composite samples.

Figure 6 shows UV–Vis diffuse reflectance spectra of the g-C<sub>3</sub>N<sub>4</sub>, ZnV<sub>2</sub>O<sub>6</sub>, ZnV<sub>2</sub>O<sub>6</sub>/g-C<sub>3</sub>N<sub>4</sub> and reduced graphene oxide/g-C<sub>3</sub>N<sub>4</sub> modified ZnV<sub>2</sub>O<sub>6</sub> nanocomposite. The reduced graphene oxide/g-C<sub>3</sub>N<sub>4</sub> modified ZnV<sub>2</sub>O<sub>6</sub> nanocomposite can improve the absorbance of g-C<sub>3</sub>N<sub>4</sub> towards visible light illuminations. The band gap energies of all photocatalysts were found from the extrapolation of Tauc plot to the abscissa of photon energy (eV). The band gap values of all photocatalysts are listed in Table 1. The wavelengths of ZnV<sub>2</sub>O<sub>6</sub>, g-C<sub>3</sub>N<sub>4</sub>, ZnV<sub>2</sub>O<sub>6</sub>/g-C<sub>3</sub>N<sub>4</sub> and reduced graphene oxide/g-C<sub>3</sub>N<sub>4</sub> modified ZnV<sub>2</sub>O<sub>6</sub> nanocomposite are 613 nm, 476 nm, 560 nm and 574 nm, respectively. Obviously, g-C<sub>3</sub>N<sub>4</sub> displays lower absorption than ZnV<sub>2</sub>O<sub>6</sub> nanosheets in the visible-light region. The wavelength regions of ZnV<sub>2</sub>O<sub>6</sub>/g-C<sub>3</sub>N<sub>4</sub> heterojunction and reduced graphene oxide/g-C<sub>3</sub>N<sub>4</sub> modified ZnV<sub>2</sub>O<sub>6</sub> nanocomposite are prolonged toward visible-light region compared with the g-C<sub>3</sub>N<sub>4</sub> sample.

In order to clarify the separation of photogenerated electron–hole pairs over the reduced graphene oxide/g-C<sub>3</sub>N<sub>4</sub> modified ZnV<sub>2</sub>O<sub>6</sub> nanocomposite, it is necessary to find out the conduction band (CB) and valence band (VB) potentials of the components. The valence band edges of treated g-C<sub>3</sub>N<sub>4</sub> and ZnV<sub>2</sub>O<sub>6</sub> photocatalyst were positioned at 1.48 eV and 1.15 eV, respectively, as shown in Fig. 6b–c and similarly reported previously [29]. The values of band gap

(E<sub>bg</sub>) for ZnV<sub>2</sub>O<sub>6</sub> photocatalyst and treated g-C<sub>3</sub>N<sub>4</sub> are (2.02 eV) and (2.6 eV), respectively. Hence, the conduction band edges of treated g-C<sub>3</sub>N<sub>4</sub> and ZnV<sub>2</sub>O<sub>6</sub> photocatalyst were calculated to be (–1.12 eV) and (–0.87 eV), respectively. The valence band edge of treated g-C<sub>3</sub>N<sub>4</sub> is lower than the valence band edge of ZnV<sub>2</sub>O<sub>6</sub> photocatalyst, and the conduction band edge of ZnV<sub>2</sub>O<sub>6</sub> photocatalyst is lower than conduction band edge of treated g-C<sub>3</sub>N<sub>4</sub>.

The charges recombination rate over pristine g-C<sub>3</sub>N<sub>4</sub>, reduced graphene oxide, ZnV<sub>2</sub>O<sub>6</sub>, ZnV<sub>2</sub>O<sub>6</sub>/g-C<sub>3</sub>N<sub>4</sub> and reduced graphene oxide/g-C<sub>3</sub>N<sub>4</sub> modified ZnV<sub>2</sub>O<sub>6</sub> photocatalysts was identified utilizing PL spectra and the results are presented in Fig. 7. The PL spectra were obtained at a wavelength of 325 nm. The ZnV<sub>2</sub>O<sub>6</sub> photocatalyst display lower emission intensity of PL spectra compared with the g-C<sub>3</sub>N<sub>4</sub> sample. After the g-C<sub>3</sub>N<sub>4</sub> was inserted, the heterostructured photocatalysts display lower PL intensity compared with the ZnV<sub>2</sub>O<sub>6</sub> photocatalyst. The peak of reduced graphene oxide/g-C<sub>3</sub>N<sub>4</sub> modified ZnV<sub>2</sub>O<sub>6</sub> nanocomposite exhibits the lowest emission intensity of PL spectra after inserting reduced graphene oxide with ZnV<sub>2</sub>O<sub>6</sub> and g-C<sub>3</sub>N<sub>4</sub>, which discloses the higher separation between the photo-generated electron and hole pairs in the reduced graphene oxide/g-C<sub>3</sub>N<sub>4</sub> modified ZnV<sub>2</sub>O<sub>6</sub> nanocomposite surface. The present results reveal that the reduced graphene oxide inserted g-C<sub>3</sub>N<sub>4</sub> modified ZnV<sub>2</sub>O<sub>6</sub> composite could provide further active charge separation than reduced graphene oxide free ZnV<sub>2</sub>O<sub>6</sub>/g-C<sub>3</sub>N<sub>4</sub> composite.

### Photocatalytic CO<sub>2</sub> conversion with H<sub>2</sub>O

The control experiments were conducted for the conversion of CO<sub>2</sub> under solar light and UV light illuminations at room temperature and feed flow rate 5 ml min<sup>–1</sup>. For this purpose two set of experiments were conducted: first, using photocatalyst and light irradiation without feed mixture, second, using feed mixture and light irradiations without loading catalyst. In all cases, no reaction occurred when either the reactants or the light illuminations were removed from the photocatalytic system. The impacts of solar light and UV-light illuminations on the photoactivity of catalysts were also investigated in a continuous reactor without catalyst or feed mixture and no carbon containing products were observed. This confirms carbon-based products were obtained during

**Figure 6** UV–vis diffuse reflectance absorbance spectra of g-C<sub>3</sub>N<sub>4</sub>, ZnV<sub>2</sub>O<sub>6</sub>, ZnV<sub>2</sub>O<sub>6</sub>/g-C<sub>3</sub>N<sub>4</sub> nanosheets, ZnV<sub>2</sub>O<sub>6</sub>/RGO/g-C<sub>3</sub>N<sub>4</sub> composite.

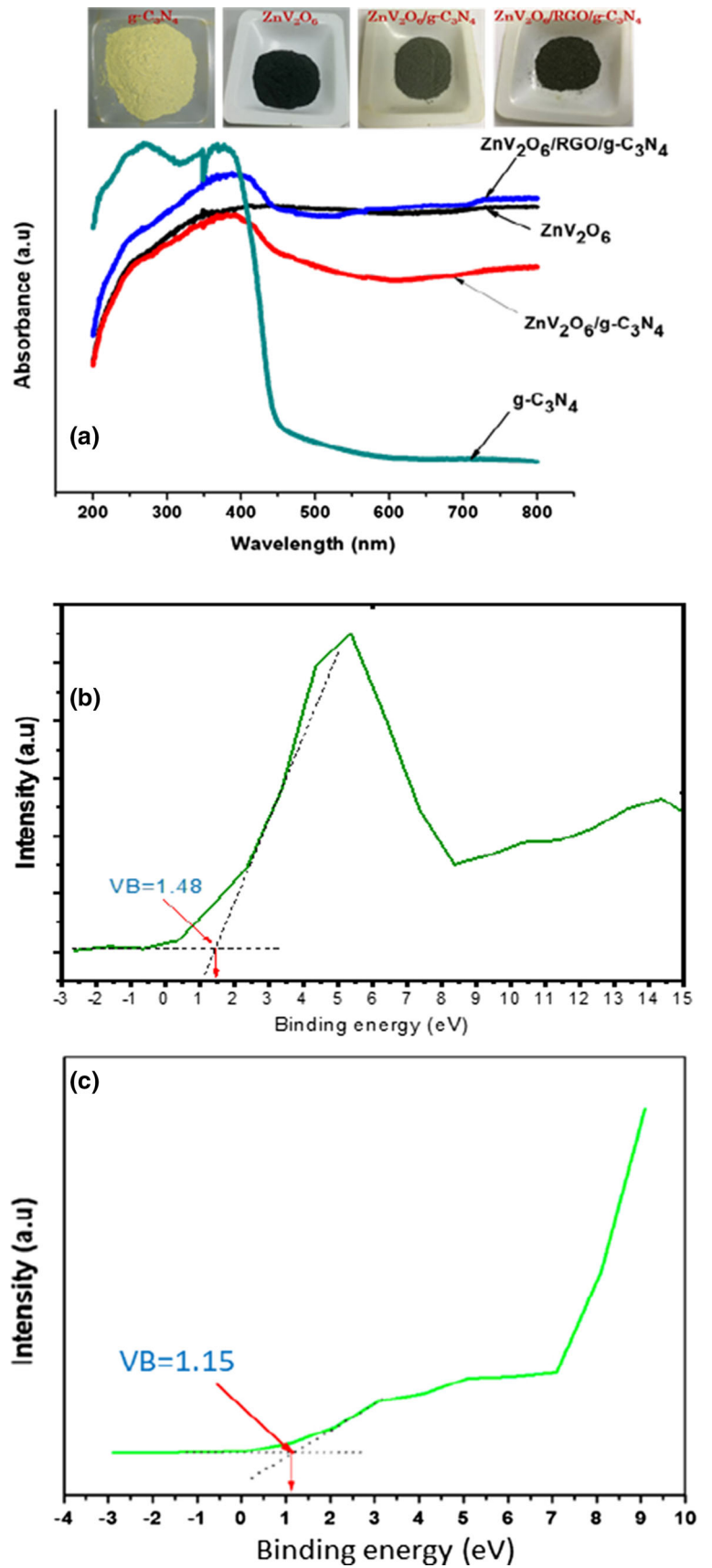
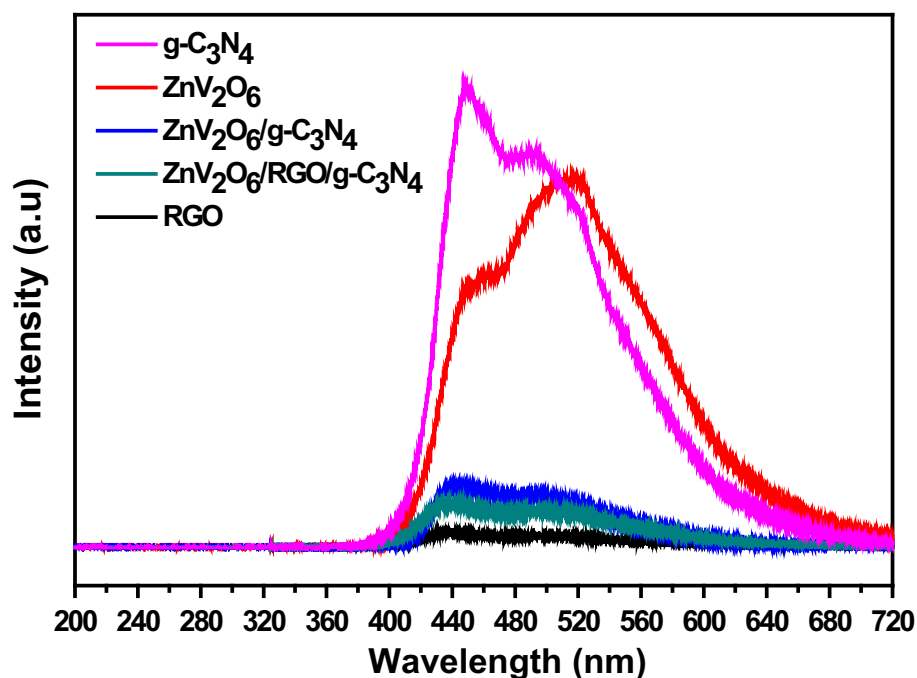


**Figure 7** Photoluminescence (PL) spectra for RGO, g-C<sub>3</sub>N<sub>4</sub>, ZnV<sub>2</sub>O<sub>6</sub>, ZnV<sub>2</sub>O<sub>6</sub>/g-C<sub>3</sub>N<sub>4</sub> and ZnV<sub>2</sub>O<sub>6</sub>/RGO/g-C<sub>3</sub>N<sub>4</sub> samples.

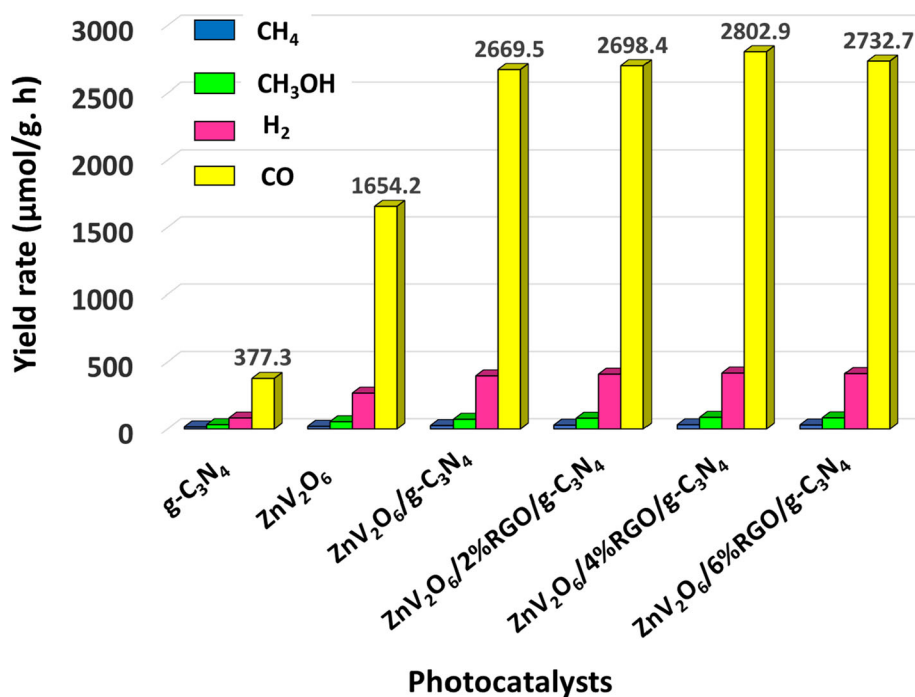


photocatalytic CO<sub>2</sub> reduction process in the presence of three components i.e., reactants, photocatalyst and light irradiation.

The effect of RGO on the efficiency of ZnV<sub>2</sub>O<sub>6</sub>/g-C<sub>3</sub>N<sub>4</sub> for photocatalytic CO<sub>2</sub> reduction with H<sub>2</sub>O to CH<sub>4</sub>, CH<sub>3</sub>OH, H<sub>2</sub> and CO under solar light irradiations is presented in Fig. 8. It is clear that the yield of

CO over ZnV<sub>2</sub>O<sub>6</sub> was higher than that over g-C<sub>3</sub>N<sub>4</sub>, which can be ascribed to the better photo absorption efficiency, efficient charge transfer property and hierarchical structure of ZnV<sub>2</sub>O<sub>6</sub> compared with g-C<sub>3</sub>N<sub>4</sub>. The efficiency of ZnV<sub>2</sub>O<sub>6</sub> was further improved when g-C<sub>3</sub>N<sub>4</sub> was loaded to get ZnV<sub>2</sub>O<sub>6</sub>/g-C<sub>3</sub>N<sub>4</sub> composite. Combined g-C<sub>3</sub>N<sub>4</sub> with ZnV<sub>2</sub>O<sub>6</sub> has

**Figure 8** Yield of CH<sub>4</sub>, CH<sub>3</sub>OH, H<sub>2</sub> and CO over various photocatalysts (irradiation time 2 h).



significantly improved photoconversion of CO<sub>2</sub> and composite ratios of 1:1 gives highest yield of products [29]. The addition of RGO into a ZnV<sub>2</sub>O<sub>6</sub>/g-C<sub>3</sub>N<sub>4</sub> developed Z-scheme heterojunction enables efficient trapping and transport of electrons. Four percent RGO was the optimal loading amounts at which the highest CO production (2802.9 μmol/g. h) was achieved. Furthermore, yields of CO declined when RGO loading exceeded 4%, probably because of the shielding influence of higher RGO contents that decreased light illumination striking the catalyst surface. Generally, significantly improved photoactivity of RGO-modified ZnV<sub>2</sub>O<sub>6</sub>/g-C<sub>3</sub>N<sub>4</sub> composite toward the conversion of CO<sub>2</sub> to CO was because of Z-scheme heterojunction, which enhances separation of electron and hole pairs and inhibits charge carrier recombination. This would also be due to more negative reduction potential of g-C<sub>3</sub>N<sub>4</sub> (−1.12 eV) compared to reduction potential of CO<sub>2</sub>/CO (−0.48 eV) production in Z-scheme heterojunction, enabling selective CO production. The detailed discussion has been included in reaction mechanism section.

The average yield rates of CO<sub>2</sub> transformation products over g-C<sub>3</sub>N<sub>4</sub>, ZnV<sub>2</sub>O<sub>6</sub>, ZnV<sub>2</sub>O<sub>6</sub>/g-C<sub>3</sub>N<sub>4</sub> and reduced graphene oxide/g-C<sub>3</sub>N<sub>4</sub> modified ZnV<sub>2</sub>O<sub>6</sub> photocatalysts under both the solar-light and UV-light are demonstrated in Fig. 9. Clearly, the generation of CO and CH<sub>3</sub>OH was significant utilizing solar light illuminations compared to UV-light under the same operating conditions. In addition, the presence of reduced graphene oxide plays an important role in efficient reduction of CO<sub>2</sub> to solar fuels. The total products significantly increased after reduced graphene oxide modified ZnV<sub>2</sub>O<sub>6</sub>/g-C<sub>3</sub>N<sub>4</sub>, whereas, largest yield of CO was 2802.9 μmol/g. h, 1.7 times larger than ZnV<sub>2</sub>O<sub>6</sub> nanosheets and 7.4-fold higher than g-C<sub>3</sub>N<sub>4</sub> nanosheets under solar light. In addition, significant amounts of CH<sub>3</sub>OH, H<sub>2</sub> and CH<sub>4</sub> were also produced, which confirms efficient production of charge carrier over the composite catalyst. These trends were the same for both solar light and UV light, however, higher amount of CO was produced under solar light. Generally, greatly enhanced photo-activity of reduced graphene oxide modified ZnV<sub>2</sub>O<sub>6</sub>/g-C<sub>3</sub>N<sub>4</sub> nanocomposite under visible light was because of Z-scheme photocatalysts with RGO as a mediator, which improves separation of hole and electron pairs and hinders charge recombination.

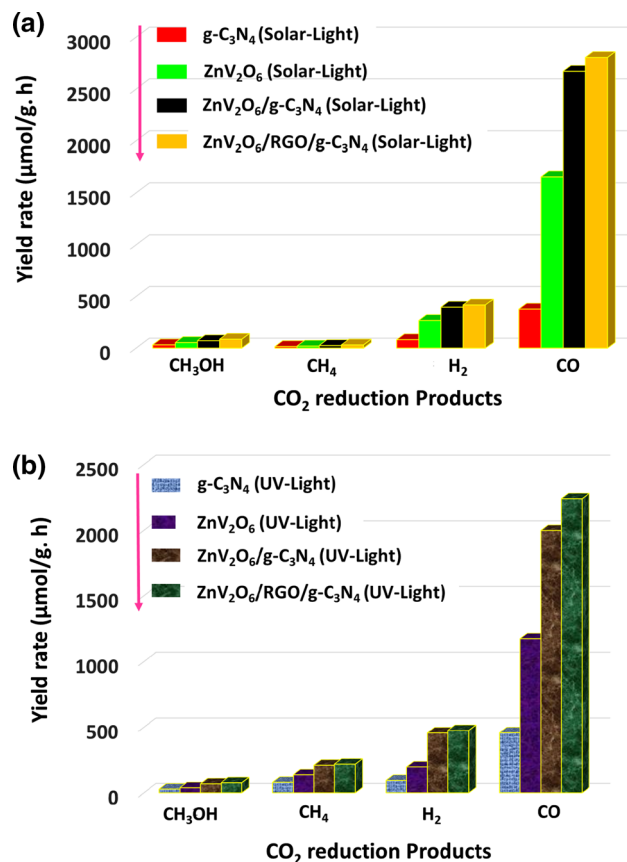


**Figure 9** Production rate of CO, CH<sub>3</sub>OH, H<sub>2</sub> and CH<sub>4</sub> during CO<sub>2</sub> reduction for various catalysts under **a** solar-light (100 mW/cm<sup>2</sup>); **b** UV-light irradiations (150 mW/cm<sup>2</sup>) (Catalyst loading 100 mg, CO<sub>2</sub> flow rate 5 mL min<sup>−1</sup>).

Under UV-light ZnV<sub>2</sub>O<sub>6</sub>/g-C<sub>3</sub>N<sub>4</sub> works as type I heterojunction, however, using visible light irradiation, indirect Z-scheme heterojunction was established. As the band gap energy of g-C<sub>3</sub>N<sub>4</sub> is higher than ZnV<sub>2</sub>O<sub>6</sub>, thus it would be activated first under UV-light and transforming electrons and holes from CB and VB of g-C<sub>3</sub>N<sub>4</sub> towards CB and VB of ZnV<sub>2</sub>O<sub>6</sub> due to difference in reduction potentials. Under visible light, an indirect Z-scheme heterojunction of ZnV<sub>2</sub>O<sub>6</sub>/g-C<sub>3</sub>N<sub>4</sub> with RGO as a solid electron mediator was established. Due to lower band gap energy of ZnV<sub>2</sub>O<sub>6</sub>, it would be activated first, transforming electrons from its CB to VB of g-C<sub>3</sub>N<sub>4</sub> through RGO. Therefore, significantly enhanced photocatalytic activity was due to indirect Z-scheme heterojunction formation with faster charge carrier separation and higher visible light absorption, resulting in significantly enhanced photocatalytic CO<sub>2</sub> reduction to CO and other products.

**Figure 10** Performance analysis of photo-catalysts for photocatalytic CO<sub>2</sub> reduction with H<sub>2</sub>O under solar-light irradiation (Catalyst loading 100 mg, CO<sub>2</sub> flow rate 5 mL min<sup>-1</sup>).

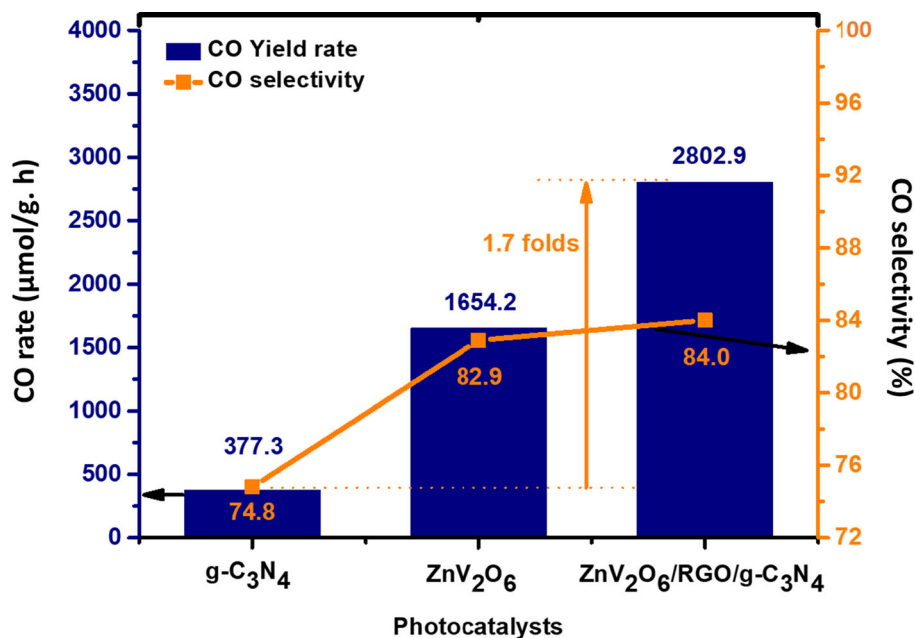


**Table 2** Summary of yield rates and selectivity of different products over g-C<sub>3</sub>N<sub>4</sub>, ZnV<sub>2</sub>O<sub>6</sub> and ZnV<sub>2</sub>O<sub>6</sub>/RGO/g-C<sub>3</sub>N<sub>4</sub> photocatalysts

Photocatalysts	Yield rate (μmol/g. h)				Selectivity (%)			
	CO	CH <sub>3</sub> OH	H <sub>2</sub>	CH <sub>4</sub>	CO	CH <sub>3</sub> OH	H <sub>2</sub>	CH <sub>4</sub>
g-C <sub>3</sub> N <sub>4</sub>	377.3	31.2	81.2	14.8	74.8	6.2	16.1	2.9
ZnV <sub>2</sub> O <sub>6</sub>	1654.2	53.7	267.3	19.2	82.9	2.7	13.4	1.0
ZnV <sub>2</sub> O <sub>6</sub> /RGO/g-C <sub>3</sub> N <sub>4</sub>	2802.9	85.9	417.5	30.6	84.0	2.6	12.5	0.9

The yield rates and selectivity of various products over the different photocatalysts during photocatalytic conversion of CO<sub>2</sub> under solar-light irradiations are presented in Fig. 10 and are tabulated in Table 2. The CO<sub>2</sub> reduction products observed were CO, CH<sub>3</sub>OH, H<sub>2</sub> and CH<sub>4</sub> over different kinds of photocatalysts. The CO yield as a main product over reduced graphene oxide/g-C<sub>3</sub>N<sub>4</sub> modified ZnV<sub>2</sub>O<sub>6</sub> nanocomposite is 2802.9 μmol/g. h, 7.4 and 1.7-fold higher than g-C<sub>3</sub>N<sub>4</sub> and ZnV<sub>2</sub>O<sub>6</sub> samples, respectively. Therefore, reduced graphene oxide/g-C<sub>3</sub>N<sub>4</sub> modified ZnV<sub>2</sub>O<sub>6</sub> nanocomposite is effective for the generation of CO. Furthermore, observed CO selectivity of 74.8% over g-C<sub>3</sub>N<sub>4</sub> increased to 82.9% and 84.0% using ZnV<sub>2</sub>O<sub>6</sub> and reduced graphene oxide/g-C<sub>3</sub>N<sub>4</sub> modified ZnV<sub>2</sub>O<sub>6</sub> catalysts, respectively. This greatly improved yield with enhanced selectivity towards CO reveals effective generation of electrons with appropriate band structure in Z-scheme based reduced graphene oxide/g-C<sub>3</sub>N<sub>4</sub> modified ZnV<sub>2</sub>O<sub>6</sub> heterojunction.

The stability of reduced graphene oxide/g-C<sub>3</sub>N<sub>4</sub> modified ZnV<sub>2</sub>O<sub>6</sub> nanocomposite was further investigated to assess the life of photocatalyst under solar-light and UV-light illuminations as shown in Fig. 11. The production of CO over reduced graphene oxide/g-C<sub>3</sub>N<sub>4</sub> modified ZnV<sub>2</sub>O<sub>6</sub> nanocomposite under solar-light and UV-light illuminations at various reaction times is discussed in Fig. 11a. The generation of CO is higher under solar-light as compared to utilizing of UV-light illuminations. In the situation of UV-light illumination, the CO yield increased and then declines over the time on stream, while using solar-light illuminations, the CO yield increased until steady state was reached. Although solar-light (100 mW cm<sup>-2</sup>) has lower light intensity than UV-light (150 mW cm<sup>-2</sup>), generation of CO was higher under solar-light illuminations. This reveals that efficiency of photocatalysts could not be improved by increasing light intensity, but absorption of light spectra is also significant for generating charge carriers during photoreduction of CO<sub>2</sub> process. Thus, higher and continuous photocatalytic CO<sub>2</sub> reduction

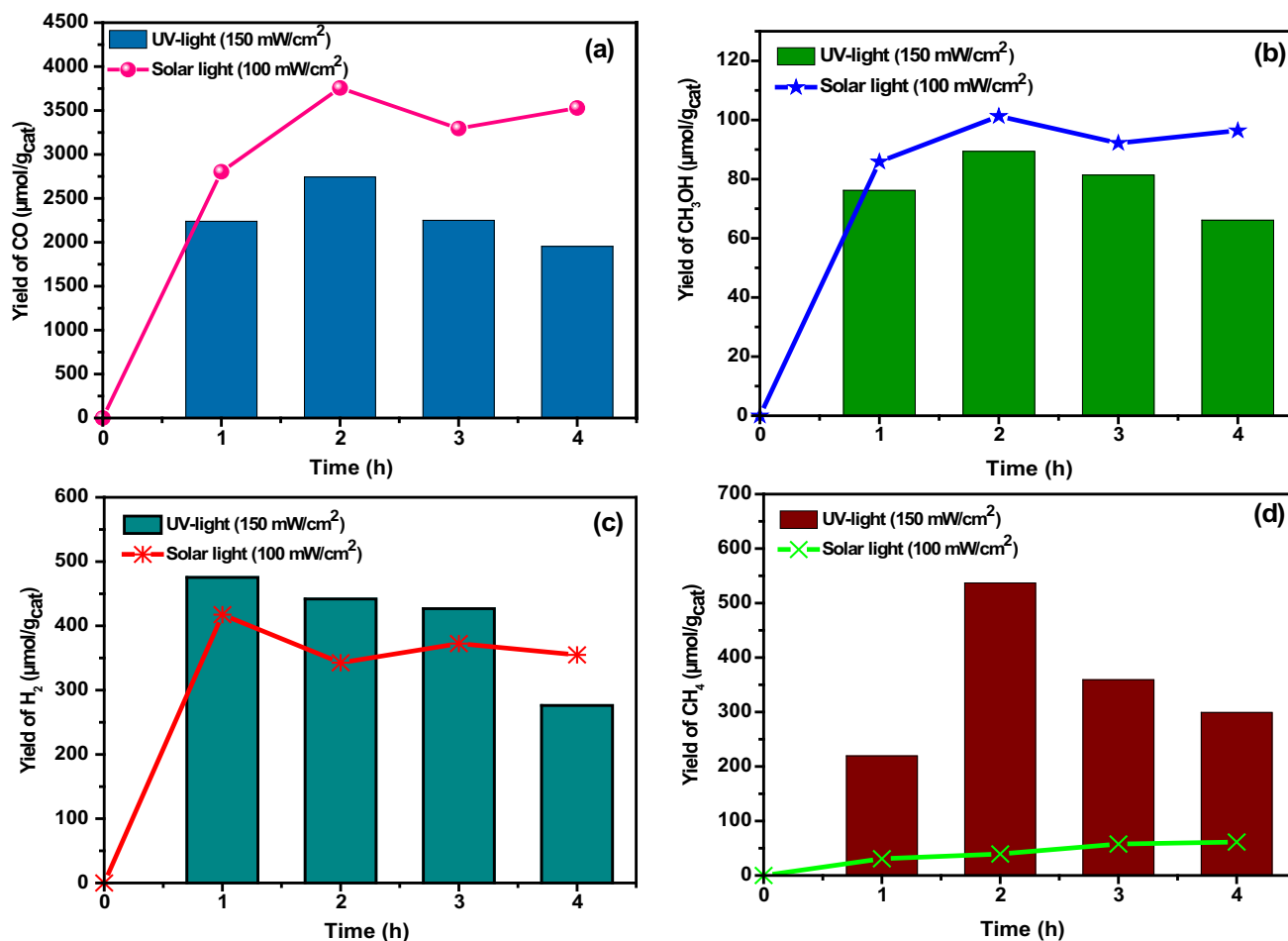


**Figure 11** Effect of irradiation time on the performance of  $\text{ZnV}_2\text{O}_6/\text{RGO}/\text{g-C}_3\text{N}_4$  composite for photocatalytic  $\text{CO}_2$  reduction under UV and visible light irradiation: **a** Yield of  $\text{CO}$ ; **b** Yield of

$\text{CH}_3\text{OH}$ ; **c** Yield of  $\text{H}_2$ ; **d** Yield of  $\text{CH}_4$  (Catalyst loading 100 mg,  $\text{CO}_2$  flow rate  $5 \text{ mL min}^{-1}$ ).

under visible light over RGO mediated  $\text{ZnV}_2\text{O}_6/\text{g-C}_3\text{N}_4$  composite was due to higher visible light absorption and faster charge carrier separation. However, under UV-light irradiation, there was not efficient light utilization, resulting in lower production of electrons, whereas, higher light intensity would also damage catalyst, resulting in declined photoactivity over the time on stream.

Figure 11b displayed the photoconversion of  $\text{CO}_2$  into  $\text{CH}_3\text{OH}$  under solar-light and UV-light illuminations. Noticeably, various amounts of  $\text{CH}_3\text{OH}$  were generated throughout photoconversion of  $\text{CO}_2$  under solar and UV light illuminations. The solar light illuminations can generate more electron and hole pairs over the reduced graphene oxide/ $\text{g-C}_3\text{N}_4$  modified  $\text{ZnV}_2\text{O}_6$  surface because of higher light absorption due to appropriate band gap energy. For the production of one mole of  $\text{CH}_3\text{OH}$ , six electrons

and six holes are required, that were effectively generated over the composite catalyst, resulting in generation of  $\text{CH}_3\text{OH}$  under solar light illuminations. The production of  $\text{H}_2$  over reduced graphene oxide/ $\text{g-C}_3\text{N}_4$  modified  $\text{ZnV}_2\text{O}_6$  nanocomposite under solar-light and UV-light illuminations during photocatalytic  $\text{CO}_2$  reduction is shown Fig. 11c. The  $\text{H}_2$  production increased at the beginning and then declines over time. However, reduced graphene oxide/ $\text{g-C}_3\text{N}_4$  modified  $\text{ZnV}_2\text{O}_6$  nanocomposite was favourable for efficient production of  $\text{H}_2$  under solar light illuminations. In the situation of UV light illumination, the  $\text{H}_2$  yield was declined due to less absorption of light irradiation and instability of catalyst using high intensity short wavelength photon energy ( $I = 150 \text{ mW cm}^{-2}$ ,  $\lambda = 254 \text{ nm}$ ).

The photocatalytic  $\text{CO}_2$  conversion to  $\text{CH}_4$  over reduced graphene oxide/ $\text{g-C}_3\text{N}_4$  modified  $\text{ZnV}_2\text{O}_6$

nanocomposite is exhibited in Fig. 11d. Evidently, the CH<sub>4</sub> yield was increased under solar-light illuminations, while it was declined over time under UV light illuminations. Besides, photo-activity of reduced graphene oxide/g-C<sub>3</sub>N<sub>4</sub> modified ZnV<sub>2</sub>O<sub>6</sub> nanocomposite was steady under solar light illuminations. This confirmed prolonged photo-activity of reduced graphene oxide/g-C<sub>3</sub>N<sub>4</sub> modified ZnV<sub>2</sub>O<sub>6</sub> nanocomposite for incessant CH<sub>4</sub> generation under solar light illuminations. In general, significantly enhanced photo-activity of reduced graphene oxide/g-C<sub>3</sub>N<sub>4</sub> modified ZnV<sub>2</sub>O<sub>6</sub> nanocomposite toward reduction of CO<sub>2</sub> was evident due to efficient charge separation, light absorption, and indirect Z-scheme assembly developed between ZnV<sub>2</sub>O<sub>6</sub> and g-C<sub>3</sub>N<sub>4</sub> through bridging layer of reduced graphene oxide.

### Quantum yield analysis

Although, yield rates calculation is promising factor to evaluate the performance of photocatalysts, however, it does not provide any information about the photon energy utilized and amount of photon consumed for the conversion of CO<sub>2</sub>. Recently, quantum yield (QY) has been considered as the most promising and reliable approach to compare the performance of different photocatalytic reactor systems. Thus, efficiency of the photocatalysts was further evaluated based on the quantum yield, calculated for each experiment, as the ratio of the production rate (μmole per sec) of specific product with photonic flux (μmole per sec) consumption. The number of moles (n) of 2, 2, 6 and 8 were used for the production of CO, H<sub>2</sub>, CH<sub>3</sub>OH and CH<sub>4</sub>. The light intensity of 100 mW cm<sup>-2</sup> at wavelength 450 nm and incident area of 36 cm<sup>2</sup> was used for QY calculation. The QY for the production of CO, CH<sub>3</sub>OH, H<sub>2</sub> and CH<sub>4</sub> over g-C<sub>3</sub>N<sub>4</sub>, ZnV<sub>2</sub>O<sub>6</sub> and RGO loaded ZnV<sub>2</sub>O<sub>6</sub>/g-C<sub>3</sub>N<sub>4</sub> composite has been demonstrated in Table 3. Using pristine g-C<sub>3</sub>N<sub>4</sub> and ZnV<sub>2</sub>O<sub>6</sub>, lower QY was obtained, which was obviously increased in ZnV<sub>2</sub>O<sub>6</sub>/g-C<sub>3</sub>N<sub>4</sub> heterojunction formation. A further enhancement in

QY was observed in RGO mediated ZnV<sub>2</sub>O<sub>6</sub>/g-C<sub>3</sub>N<sub>4</sub> composite. The maximum apparent yield for CO of 0.115% was achieved over reduced graphene oxide/g-C<sub>3</sub>N<sub>4</sub> modified ZnV<sub>2</sub>O<sub>6</sub> composite under visible light irradiation, which is 1.7 and 7.6 folds higher than using ZnV<sub>2</sub>O<sub>6</sub> and g-C<sub>3</sub>N<sub>4</sub> samples, respectively. Among the other products, QY for H<sub>2</sub> was higher than CH<sub>3</sub>OH and CH<sub>4</sub> production, which confirms both CO<sub>2</sub> reduction and water reaction were competing over the ZnV<sub>2</sub>O<sub>6</sub>/RGO/g-C<sub>3</sub>N<sub>4</sub> composite catalyst surface. The performance of current study was further compared with literature, but there are limited reports are available. Photocatalytic CO<sub>2</sub> reduction to CO and CH<sub>4</sub> with QY of 0.0099% over g-C<sub>3</sub>N<sub>4</sub> coupled with alkaline Ti<sub>3</sub>C<sub>2</sub> MXene composite under visible light has been reported [45]. Previously, we reported a QY of 0.028 and 0.0028% for CO and CH<sub>3</sub>OH production over ZnV<sub>2</sub>O<sub>6</sub>/pCN composite under visible light irradiation [25]. In the current work, the significantly enhanced photocatalytic performance of RGO mediated ZnV<sub>2</sub>O<sub>6</sub>/g-C<sub>3</sub>N<sub>4</sub> for photocatalytic CO<sub>2</sub> conversion was obviously due to Z-scheme heterojunction formation with superior charge carrier transportation and higher visible light absorption.

$$*QY, (\%) = \frac{n \times \text{production rate } (\mu\text{mol/sec})}{\text{photon flux } (\mu\text{mol/sec})} \times 100,$$

where,  $n = 2, 2, 6$  and  $8$  for CO, H<sub>2</sub>, CH<sub>3</sub>OH and CH<sub>4</sub> production;  $I = 100 \text{ mW cm}^{-2}$ ,  $\lambda = 450 \text{ nm}$ .

In order to examine the performance of ZnV<sub>2</sub>O<sub>6</sub>/RGO/g-C<sub>3</sub>N<sub>4</sub> composite for photocatalytic CO<sub>2</sub> reduction, results are further compared with the work reported by many researchers as displayed in Table 4 Ga<sub>2</sub>O<sub>3</sub> was investigated for photo-induced CO<sub>2</sub> conversion under UV-light irradiations and the products obtained was CO with production rate of 3.82 μmol/g. h [50]. Similarly, Au/TNTs was used for photoconversion of CO<sub>2</sub> and the product obtained was CO with production rate of 11.9 μmol/g. h [51]. Another work, Cu<sub>2</sub>V<sub>2</sub>O<sub>7</sub>/g-C<sub>3</sub>N<sub>4</sub> was used for reduction of CO<sub>2</sub> and the product obtained was CO

**Table 3** Quantum yield of g-C<sub>3</sub>N<sub>4</sub>, ZnV<sub>2</sub>O<sub>6</sub> and RGO modified composite samples using visible light irradiation

Photocatalysts	Production rate (μmol/g. h)				Quantum yield, QY (%)			
	CO	CH <sub>3</sub> OH	H <sub>2</sub>	CH <sub>4</sub>	CO	CH <sub>3</sub> OH	H <sub>2</sub>	CH <sub>4</sub>
g-C <sub>3</sub> N <sub>4</sub>	37.73	3.12	8.12	1.48	0.015	0.004	0.003	0.002
ZnV <sub>2</sub> O <sub>6</sub>	165.42	5.37	26.73	1.92	0.068	0.007	0.011	0.003
ZnV <sub>2</sub> O <sub>6</sub> /RGO/g-C <sub>3</sub> N <sub>4</sub>	280.29	8.59	41.75	3.06	0.115	0.011	0.017	0.005



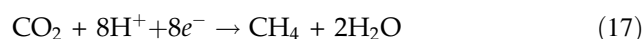
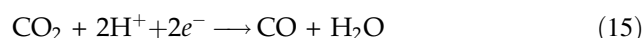
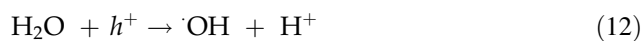
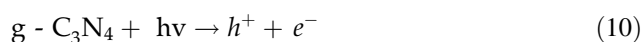
**Table 4** Summary of photocatalysts used for CO<sub>2</sub> reduction to fuels with the reported values in the literature

Catalysts	Catalyst Used	Light Source	Production rate (μmol/g. h) CO	Ref
ZnV <sub>2</sub> O <sub>6</sub> /RGO/g-C <sub>3</sub> N <sub>4</sub>	0.1 g	LCS 100, Solar simulator (100 mW/cm <sup>2</sup> )	280.29	Current Study
Ga <sub>2</sub> O <sub>3</sub>	0.2 g	300 W Xe-Lamp, 9 mW/cm <sup>2</sup>	3.82	[50]
Au/TNTs	0.15 g	AM 1.5G sunlight	11.9	[51]
Pt/TiO <sub>2</sub>	0.2 g	500 W Xe-lamp	150	[54]
Cu <sub>2</sub> V <sub>2</sub> O <sub>7</sub> /g-C <sub>3</sub> N <sub>4</sub>	0.2 g	20 W white bulbs	166	[52]
Ni-SA-x/ZrO <sub>2</sub>	0.15 g	500 W Xe-lamp	11.8	[53]

(166 μmol/g. h) under UV-light irradiations [52]. Recently, Ni-SA-x/ZrO<sub>2</sub> was reported for conversion of CO<sub>2</sub> under UV-light irradiation. The product observed was CO with production rate of 11.8 μmol/g. h [53]. By comparing all the results with the current study, it is evident that production rate of CO during photoconversion of CO<sub>2</sub> was much higher over ZnV<sub>2</sub>O<sub>6</sub>/RGO/g-C<sub>3</sub>N<sub>4</sub> nanocatalysts under visible light irradiations. Thus, the efficiency and selectivity of CO production can be improved for photocatalytic CO<sub>2</sub> conversion with 2D/2D/2D heterojunction of graphene oxide mediated g-C<sub>3</sub>N<sub>4</sub> and ZnV<sub>2</sub>O<sub>6</sub> composite. In general, better performance was due to efficient charge separation, light absorption and the ability of RGO as a mediator to act as an electron trapping agent.

### Mechanism of reaction

In order to understand the improved efficiency of reduced graphene oxide/g-C<sub>3</sub>N<sub>4</sub> modified ZnV<sub>2</sub>O<sub>6</sub> nanocomposite for the generation of CO, CH<sub>3</sub>OH, H<sub>2</sub> and CH<sub>4</sub> during photoinduced conversion of CO<sub>2</sub> with water under reaction system of pH ~ 7, following reaction mechanism can be established as described in Eqs. (9–17) [16, 25, 46].



The generation of excited hole and electron pairs and their trapping via reduced graphene oxide are presented in Eqs. (9–11). The photoreduction of CO<sub>2</sub> occurs at the CB via the electrons, while H<sub>2</sub>O is oxidized via holes at the VB and this is described in Eqs. (12) and (13). The generation of CO, CH<sub>3</sub>OH, H<sub>2</sub> and CH<sub>4</sub> during the photoconversion of CO<sub>2</sub> is exhibited in Eqs. (14–17).

The ZnV<sub>2</sub>O<sub>6</sub> and g-C<sub>3</sub>N<sub>4</sub> are irradiated to generate the electrons and holes under UV and visible light irradiation. Under UV-light irradiation, g-C<sub>3</sub>N<sub>4</sub> was first activated due to its higher band gap energy ( $E_{\text{bg}} \sim 2.6$  eV), producing electrons and holes at CB and VB band positions. Since the conduction band of ZnV<sub>2</sub>O<sub>6</sub> photocatalyst (−0.87 eV) is lower than the conduction band of g-C<sub>3</sub>N<sub>4</sub> photocatalyst (−1.12 eV), thus photo-excited electrons from CB of g-C<sub>3</sub>N<sub>4</sub> photocatalyst can be transferred towards the CB of ZnV<sub>2</sub>O<sub>6</sub> photocatalyst, enabling faster charge carrier separation. However, ZnV<sub>2</sub>O<sub>6</sub>/g-C<sub>3</sub>N<sub>4</sub> heterojunction featured the type-I band alignment charge transport procedure, which decreases the redox capability of the systems. Hence, unavoidably reducing the photocatalytic performance of the ZnV<sub>2</sub>O<sub>6</sub>/g-C<sub>3</sub>N<sub>4</sub> hetero-junctions as shown in Fig. 12a. Introducing RGO in this heterojunction would only trap electrons and transfer towards CO<sub>2</sub> for its reduction.

Under visible light irradiation, ZnV<sub>2</sub>O<sub>6</sub> will be first irradiated, producing electrons and holes. Due to lower CB of ZnV<sub>2</sub>O<sub>6</sub> (−0.87) compared to g-C<sub>3</sub>N<sub>4</sub> CB

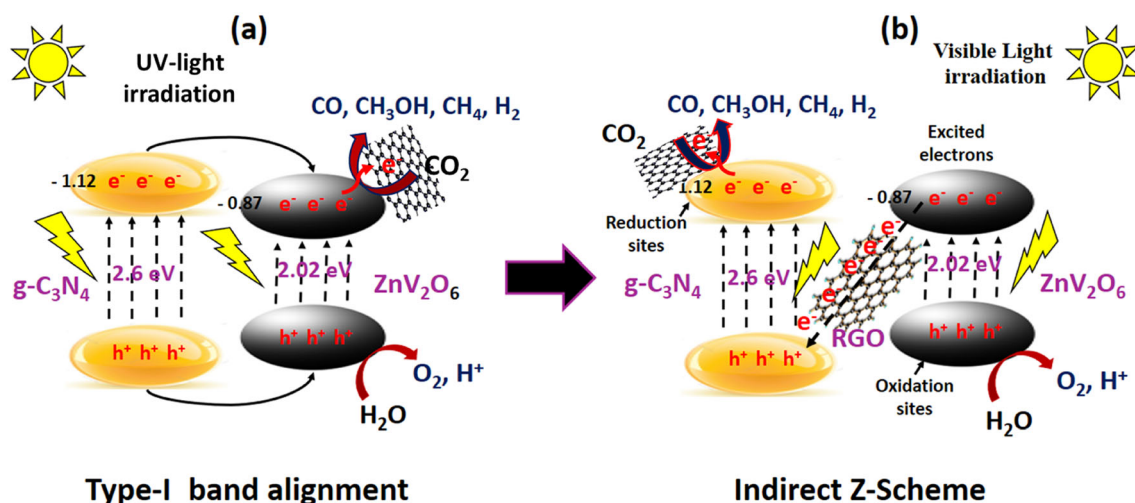


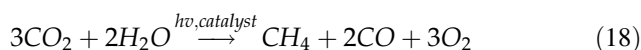
**Figure 12** Schematic illustration of photocatalytic CO<sub>2</sub> reduction over RGO/ZnV<sub>2</sub>O<sub>6</sub>/g-C<sub>3</sub>N<sub>4</sub> composite under UV and visible light irradiations **a** Type-I band alignment mechanism of ZnV<sub>2</sub>O<sub>6</sub>/RGO/

g-C<sub>3</sub>N<sub>4</sub> composite under UV-light, and **b** Z-scheme electron transfer mechanism of ZnV<sub>2</sub>O<sub>6</sub>/RGO/g-C<sub>3</sub>N<sub>4</sub> composite under visible light.

(−1.12 eV), electrons are unable to transfer from CB-to-CB positions. However, they have potential to be transferred from CB of ZnV<sub>2</sub>O<sub>6</sub> CB to VB of g-C<sub>3</sub>N<sub>4</sub>, thus constructing Z-scheme heterojunction with efficient charge transfer and separation. Introducing reduced graphene oxide to ZnV<sub>2</sub>O<sub>6</sub>/g-C<sub>3</sub>N<sub>4</sub> nanocomposite provides indirect Z-scheme heterostructure, which would be beneficial for promoting charges separation as shown in Fig. 12b. In such type of systems RGO would have dual functions, it can trap electrons from g-C<sub>3</sub>N<sub>4</sub> and transferred towards CO<sub>2</sub> for its reduction. In addition, reduced graphene oxide as a mediator obviously delivers effective channels to foster electron transfer with great mobility among g-C<sub>3</sub>N<sub>4</sub> and ZnV<sub>2</sub>O<sub>6</sub> photocatalysts. The capability of electron transport of reduced graphene oxide from ZnV<sub>2</sub>O<sub>6</sub> photocatalyst CB edge to g-C<sub>3</sub>N<sub>4</sub> photocatalyst VB edge for the reduced graphene oxide/g-C<sub>3</sub>N<sub>4</sub> modified ZnV<sub>2</sub>O<sub>6</sub> was stronger than the ZnV<sub>2</sub>O<sub>6</sub>/g-C<sub>3</sub>N<sub>4</sub> [55]. Nevertheless, in this Z-Scheme heterostructure, the photoproduced electrons in the conduction band edge of ZnV<sub>2</sub>O<sub>6</sub> photocatalyst can be transported faster to the valence band edge of g-C<sub>3</sub>N<sub>4</sub> photocatalyst via reduced graphene oxide and recombine with photoproduced holes, which efficiently decrease the recombination of photoproduced charge carriers.

### Development of kinetic model

In heterogeneous photocatalysis, reaction rates of surface are dependent on the fraction of active sites that are covered by the species surrounding the catalyst. In an irreversible bimolecular reaction, the rate of reaction of molecules that are competitively adsorbed on the same species of active sites depends on the probability of closeness of molecules to the adjacent sites. Moreover, this possibility may also be proportionate to the product fractional coverage. The bimolecular photo-induced reaction for CO<sub>2</sub> conversion can be described by utilizing Eq. (18) [56].



As discussed in the methodology of this study, some of the products would photoadsorb on the surface of photocatalyst and displayed down the photoreduction of CO<sub>2</sub> process. Another probability is some of the products recombined in a reversed reaction. The kinetic model is developed utilizing these assumptions to investigate the coupled influence of adsorptive photocatalytic conversion and oxidation processes. By assuming products and reactants are adsorbed on same active sites, the rate of Eq. (18) could be determined utilizing L–H model as depicted in Eq. (19).

$$r_s = k_s I^a \left( \frac{K_{CO_2} P_{CO_2} K_{H_2O} P_{H_2O}}{(1 + K_{CO_2} P_{CO_2} + K_{H_2O} P_{H_2O} + K_{CH_4} P_{CH_4} + K_{CO} P_{CO} + K_{O_2} P_{O_2})^3} \right) - k_{-s} I_{-s}^a \left( \frac{K_{CH_4} P_{CH_4} K_{CO} P_{CO} K_{O_2} P_{O_2}}{(1 + K_{CO_2} P_{CO_2} + K_{H_2O} P_{H_2O} + K_{CH_4} P_{CH_4} + K_{CO} P_{CO} + K_{O_2} P_{O_2})^3} \right) \tag{19}$$

where  $r_s$  is the rate of surface reaction,  $k$  and  $k_{-s}$  are the rate constants,  $I$  and  $I_{-s}$  is the UV light or visible light flux intensity for which kinetic constants is evaluated and “ $a$ ” is the reaction order of light intensity having value 1 or less depending on the light intensity [57],  $K_{CO_2}$ ,  $K_{H_2O}$ ,  $K_{CH_4}$ ,  $K_{CO}$  and  $K_{O_2}$  are the ratios of adsorption to desorption equilibrium rate constants for  $CO_2$ ,  $H_2O$ ,  $CH_4$ ,  $CO$  and  $O_2$ , respectively.

A simple kinetic model incorporating the coupled influence of the adsorptive photoinduced oxidation and reduction could be established utilizing the modified L–H model. During photocatalytic reduction of  $CO_2$  over the surface of photocatalyst, the rate equation can be obtained with the assumptions. If the adsorption of  $H_2O$ ,  $O_2$  and  $CH_4$  is considered weak over the photocatalyst, while the catalyst surface is surplus with  $CO_2$  and  $CO$ , then the rate equation becomes Eq. (20)

$$\text{Rate of Reduction} = k I^a \frac{K_{H_2O} P_{H_2O} K_{CO_2} P_{CO_2}}{(1 + K_{CO_2} P_{CO_2} + K_{CO} P_{CO})^3} \tag{20}$$

Utilizing the following assumptions, the rate of conversion in Eq. (20) is simplified to Eq. (21).

- a) The  $CO_2$  conversion on the surface leads to production of  $CO$  which is desorbed or finally converted to other products such as  $CH_3OH$  and  $CH_4$  through the involvement of electrons and holes. Therefore, rate of  $CO_2$  conversion is dependent on  $CO$  desorption or its conversion to other products. Thus, catalyst surface should be surplus with  $CO$  and rate of reaction is dependent on its formation.
- b) The rate of reaction should be very fast in the beginning but declined with time due to the accumulation of  $CO$  on the catalyst surface, thus covering active sites. Any enhancement on rate of reaction should be dependent on  $CO$  desorption or its conversion to gaseous products such

as  $CH_3OH$  or  $CH_4$  to make available more active sites for  $CO_2$  adsorption. If surface is accumulated with  $CO$  due to its attachment with active sites, i.e.  $K_{CO} P_{CO} \gg 1 + K_{CO_2} P_{CO_2}$ , then Eq. 20 can be simplified to get Eq. (21).

$$\text{Rate of reduction} = k_1 \frac{K_{H_2O} P_{H_2O} K_{CO_2} P_{CO_2}}{(K_{CO} P_{CO})^3} \tag{21}$$

where,  $k_1 = (k I^a)$  is the photoconversion rate constant influenced by light intensity and temperature.

The rate of product formation depends on reduction or/and desorption of  $CO$  over the catalyst surface; when the photocatalyst surface is surplus with  $CO$ , the partial oxidation with oxygen also takes place. The L–H model could also be employed for the evaluation of rate of oxidation. When dissociative adsorption process of  $CO$  oxidation reaction with oxygen takes place, the L–H model could be written as in Eq. (22) where,  $k_2 = k_{-s} C_1^3$ .

$$\text{Rate of oxidation} = k_2 \frac{K_{CH_4} P_{CH_4} K_{CO} P_{CO} \sqrt{K_{O_2} P_{O_2}}}{(K_{CO} P_{CO})^3} \tag{22}$$

The rate of formation of the product can be obtained through the subtraction of rate of oxidation from rate of conversion as described in Eq. (23)

$$\text{Rate of formation} = k_1 \frac{K_{H_2O} P_{H_2O} K_{CO_2} P_{CO_2}}{(K_{CO} P_{CO})^3} - k_2 \frac{K_{CH_4} P_{CH_4} K_{CO} P_{CO} \sqrt{K_{O_2} P_{O_2}}}{(K_{CO} P_{CO})^3} \tag{23}$$

The partial pressure of  $CO_2$  and  $H_2O$  vapors remains constant by keeping temperature and pressure constant. Likewise, the partial pressures of  $CO$  and oxygen would be proportional to partial pressure of the desired products, i.e.  $P_{H_2O} = P_{CO_2} = P_{CH_4} = P_{CO} = P_{O_2} = P$ . On the basis of these assumptions,

product formation Eq. (23) in simplified form can be represented by Eqs. (24–26).

$$\frac{dP}{dt} = k_3 \left( \frac{P^2}{P^3} \right) - k_4 \left( \frac{P^{5/2}}{P^3} \right) \quad (24)$$

$$\frac{dP}{dt} = \left( \frac{k_3}{P} \right) - \left( \frac{k_4}{P^{1/2}} \right) \quad (25)$$

$$dt = \left( \frac{P}{k_3 - k_4 P^{1/2}} \right) dP \quad (26)$$

where,

$$k_3 = k_1 \left( \frac{K_{CO_2} K_{H_2O}}{K_{CO}} \right), \quad k_4 = k_2 \left( \frac{K_{CH_4} K_{CO} \sqrt{K_{O_2}}}{K_{CO}} \right)$$

The differential Eq. (26) was solved utilizing integral approach as displayed in Eq. (27).

$$t = -\frac{2k_3^3}{3k_4^4} \ln(k_3 - k_4 P^{1/2}) - \frac{2P^{3/2}}{3k_4} - \frac{k_3 P}{k_4^2} - \frac{2k_3^2 P^{1/2}}{k_4^2} + C \quad (27)$$

Constant C could be calculated by applying initial boundary condition ( $t \rightarrow t_0$ ,  $P_0 = 0$ ), where  $t_0$  is the startup time of reaction or time delay of photoactivities because of transient state at which  $P_0 = 0$ . By inserting the value of C in Eq. (27), Eq. (28) is found which was further simplified to Eq. (29).

$$t - t_0 = -\left( \frac{2k_3^3}{3k_4^4} \right) \ln \left( 1 - \left( \frac{P}{(k_3/k_4)^2} \right)^{1/2} \right) - \left( \frac{2}{3k_4} \right) P^{3/2} - \left( \frac{k_3}{k_4^2} \right) P - \left( \frac{2k_3^2}{k_4^2} \right) P^{1/2} \quad (28)$$

$$t - t_0 = -k_5 \ln \left( 1 - \left( \frac{P}{k_6} \right)^{1/2} \right) - (P^{3/2}) \left( k_7 + \frac{k_8}{\sqrt{P}} + \frac{k_9}{P} \right) \quad (29)$$

where,

$$k_5 = \left( \frac{2k_3^3}{3k_4^4} \right), \quad k_6 = \left( \frac{k_3}{k_4} \right)^2, \quad k_7 = \left( \frac{2}{3k_4} \right), \quad k_8 = \left( \frac{k_3}{k_4^2} \right), \quad k_9 = \left( \frac{2k_3^2}{k_4^2} \right)$$

Equation (29) is named as the kinetic Equation that could be utilized to evaluate experimental data. Nevertheless, assuming  $k_5 = (k_7 + (k_8/P^{1/2}) + (k_9/P))$ , the simplified time dependent model has been explained in Eq. (30).

$$t = t_0 - k_5 \ln \left( 1 - \left( \frac{P}{k_6} \right)^{1/2} \right) \quad (30)$$

**Table 5** Summary of kinetic constants for fitting kinetic model with experimental data

Photocatalyst	Light	Products	$K_5$	$K_6$
ZnV <sub>2</sub> O <sub>6</sub> /RGO/g-C <sub>3</sub> N <sub>4</sub>	Solar-light	CO	23.8	722.3
ZnV <sub>2</sub> O <sub>6</sub> /RGO/g-C <sub>3</sub> N <sub>4</sub>	UV-light	CO	13.9	2312.2

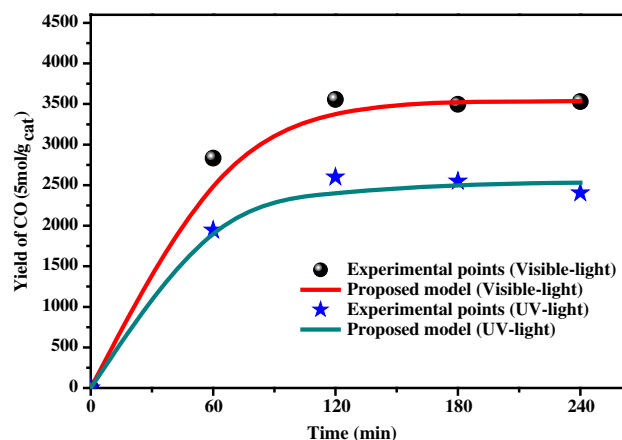


**Figure 13** Comparison of the proposed kinetic model fitting-well with the empirical profile of CO formation from photocatalytic CO<sub>2</sub> reduction with H<sub>2</sub>O.

where  $k_5$  and  $k_6$  are the kinetic constants and P is the product yield at any t time interval. This kinetic model is possibly appropriate for majority of the photocatalytic CO<sub>2</sub> conversion procedures in which there is strong movement of electrons at the photocatalyst surface and effective CO reduction to other products or CO desorption from the surface of photocatalyst.

The curves that represent the profiles of CO production over reduced graphene oxide/g-C<sub>3</sub>N<sub>4</sub> modified ZnV<sub>2</sub>O<sub>6</sub> nanocomposite as a function of irradiation time utilizing the proposed kinetic model (Eq. (30)) to fit with the experimental data utilizing the values of  $k_5$  and  $k_6$  are listed in Table 5. The profiles of CO formation for the model proposed and experimental data are displayed in Fig. 13. After insertion of the constants, the model fitted well with the experimental data. The excellent fitting of the model with experimental data confirmed strong CO presence over the surface of composite photocatalyst and/or CO<sub>2</sub> is first converted to CO and then it is desorbed or converted to other products such as CH<sub>3</sub>OH and CH<sub>4</sub> with the involvements of electrons and protons. More importantly, model can be applied under UV and visible light irradiations to estimate

the production of CO and other hydrocarbon products over time on stream under the condition of high stability of photocatalyst.

## Conclusions

In summary, the Z-scheme reduced graphene oxide/g-C<sub>3</sub>N<sub>4</sub> modified ZnV<sub>2</sub>O<sub>6</sub> nanocomposite has been successfully prepared by utilizing a one-pot solvothermal procedure and shows excellent photocatalytic CO<sub>2</sub> reduction to CO, CH<sub>3</sub>OH and CH<sub>4</sub> under solar light illumination. The reduced graphene oxide/g-C<sub>3</sub>N<sub>4</sub> modified ZnV<sub>2</sub>O<sub>6</sub> nanocomposite found very highly efficient for the production of CO with prolonged stability. CO yield rate as the main product over reduced graphene oxide/g-C<sub>3</sub>N<sub>4</sub> modified ZnV<sub>2</sub>O<sub>6</sub> nanocomposite was 2802.9 μmol/g. h, significantly higher than using g-C<sub>3</sub>N<sub>4</sub>, ZnV<sub>2</sub>O<sub>6</sub> and binary ZnV<sub>2</sub>O<sub>6</sub>/g-C<sub>3</sub>N<sub>4</sub> catalysts under solar-light illuminations. The amount of CO generated under solar-light illuminations was 1.3-times more than the amount generated utilizing UV-light illuminations. The observed CO selectivity of 74.8% over g-C<sub>3</sub>N<sub>4</sub> increased to 82.9% and 84.0% using ZnV<sub>2</sub>O<sub>6</sub> and reduced graphene oxide/g-C<sub>3</sub>N<sub>4</sub> modified ZnV<sub>2</sub>O<sub>6</sub> samples, respectively. The improved photocatalytic activity and stability over reduced graphene oxide/g-C<sub>3</sub>N<sub>4</sub> modified ZnV<sub>2</sub>O<sub>6</sub> nanocomposite can be attributed to the Z-scheme charge transfer mechanism utilizing reduced graphene oxide as effective electron mediator between the g-C<sub>3</sub>N<sub>4</sub> and ZnV<sub>2</sub>O<sub>6</sub> photocatalysts. This work indicates that indirect Z-scheme heterojunction materials could be utilized as a promising photoinduced for the CO<sub>2</sub> conversion to solar fuels. A kinetic model simulating the product formations through photocatalytic CO<sub>2</sub> conversion with H<sub>2</sub>O on the surface of reduced graphene oxide/g-C<sub>3</sub>N<sub>4</sub> modified ZnV<sub>2</sub>O<sub>6</sub> nanocomposite has been developed. The experimental data were utilized to validate the model and they fitted well with proposed model.

## Acknowledgements

The authors would like to extend their deepest appreciation to University Technology Malaysia for financial support of this research under Fundamental

Research (UTMFR, Q.J130000.2551.21H66) and Long Term Research Grant Scheme (LRGS, Vot R.J130000.7851.4L900).

## References

- [1] Tahir M, Tahir B (2020) 2D/2D/2D O-C<sub>3</sub>N<sub>4</sub>/Bt/Ti<sub>3</sub>C<sub>2</sub>Tx heterojunction with novel MXene/clay multi-electron mediator for stimulating photo-induced CO<sub>2</sub> reforming to CO and CH<sub>4</sub>. *Chem Eng J*. <https://doi.org/10.1016/j.cej.2020.125868>
- [2] Tahir M (2020) Enhanced photocatalytic CO<sub>2</sub> reduction to fuels through bireforming of methane over structured 3D MAX Ti<sub>3</sub>AlC<sub>2</sub>/TiO<sub>2</sub> heterojunction in a monolith photoreactor. *J CO<sub>2</sub>Util* 38:99–112. <https://doi.org/10.1016/j.jcou.2020.01.009>
- [3] Bafaqeer A, Tahir M, Amin NAS (2018) Synergistic effects of 2D/2D ZnV<sub>2</sub>O<sub>6</sub>/RGO nanosheets heterojunction for stable and high performance photo-induced CO<sub>2</sub> reduction to solar fuels. *Chem Eng J* 334:2142–2153
- [4] Yadav RK, Kumar A, Yadav D, Park NJ, Kim JY, Baeg JO (2018) In situ prepared flexible 3D polymer film photocatalyst for highly selective solar fuel production from CO<sub>2</sub>. *Chem Cat Chem* 10:2024–2029
- [5] Kumar A, Prajapati PK, Pal U, Jain SL (2018) A ternary rGO/InVO<sub>4</sub>/Fe<sub>2</sub>O<sub>3</sub> Z-scheme heterostructured photocatalyst for CO<sub>2</sub> reduction under visible light irradiation. *ACS Sustain Chem Eng* 6(7):820–8211
- [6] Chakraborty S, Nayak J, Ruj B, Pal P, Kumar R, Banerjee S et al (2020) Photocatalytic conversion of CO<sub>2</sub> to methanol using membrane-integrated green approach: a review on capture, conversion and purification. *J Environ Chem Eng* 8:103935. <https://doi.org/10.1016/j.jece.2020.103935>
- [7] Inoue T, Fujishima A, Konishi S, Honda K (1979) Photoelectrocatalytic reduction of carbon dioxide in aqueous suspensions of semiconductor powders. *Nature* 277:637–638
- [8] Tahir M, Tahir B, Amin NAS, Muhammad A (2016) Photocatalytic CO<sub>2</sub> methanation over NiO/In<sub>2</sub>O<sub>3</sub> promoted TiO<sub>2</sub> nanocatalysts using H<sub>2</sub>O and/or H<sub>2</sub> reductants. *Energy Convers Manage* 119:368–378
- [9] She H, Wang Y, Zhou H, Li Y, Wang L, Huang J et al (2019) Preparation of Zn<sub>3</sub>In<sub>2</sub>S<sub>6</sub>/TiO<sub>2</sub> for enhanced CO<sub>2</sub> photocatalytic reduction activity via Z-scheme electron transfer. *Chem Cat Chem* 11:753–759
- [10] Nie N, He F, Zhang L, Cheng B (2018) Direct Z-scheme PDA-modified ZnO hierarchical microspheres with enhanced photocatalytic CO<sub>2</sub> reduction performance. *Appl Surf Sci* 457:1096–1102

- [11] Ding S, Han M, Dai Y, Yang S, Mao D, He H et al (2019) Synthesis of Ag/AgBr/Bi<sub>4</sub>O<sub>5</sub>Br<sub>2</sub> plasmonic heterojunction photocatalysts: elevated visible-light photocatalytic performance and Z-scheme mechanism. *Chem Cat Chem* 11:3490–3504
- [12] Zhang Y, Sun K, Wu D, Xie W, Xie F, Zhao X et al (2019) Localized surface plasmon resonance enhanced photocatalytic activity via MoO<sub>2</sub>/BiOBr nanohybrids under visible and NIR light. *Chem Cat Chem* 11:2546–2553
- [13] Umer M, Tahir M, Usman Azam M, Tasleem S, Abbas T, Muhammad A (2019) Synergistic effects of single/multi-walls carbon nanotubes in TiO<sub>2</sub> and process optimization using response surface methodology for photo-catalytic H<sub>2</sub> evolution. *J Environ Chem Eng* 7:103361. <https://doi.org/10.1016/j.jece.2019.103361>
- [14] Khatun F, Abd Aziz A, Sim LC, Monir MU (2018) Plasmonic enhanced Au decorated TiO<sub>2</sub> nanotube arrays as a visible light active catalyst towards photocatalytic CO<sub>2</sub> conversion to CH<sub>4</sub>. *J Environ Chem Eng* 7:103233. <https://doi.org/10.1016/j.jece.2019.103233>
- [15] Fu J, Yu J, Jiang C, Cheng B (2018) g-C<sub>3</sub>N<sub>4</sub>-Based Heterostructured photocatalysts. *Adv Energy Mater* 8:1701503
- [16] Tahir B, Tahir M, Amin NAS (2019) Silver loaded protonated graphitic carbon nitride (Ag/pg-C<sub>3</sub>N<sub>4</sub>) nanosheets for stimulating CO<sub>2</sub> reduction to fuels via photocatalytic bi-reforming of methane. *Appl Surf Sci* 493:18–31
- [17] Ghafoor S, Inayat A, Aftab F, Duran H, Kirchoff K, Waseem S et al (2019) TiO<sub>2</sub> nanofibers embedded with g-C<sub>3</sub>N<sub>4</sub> nanosheets and decorated with Ag nanoparticles as Z-scheme photocatalysts for environmental remediation. *J Environ Chem Eng* 7:103452. <https://doi.org/10.1016/j.jece.2019.103452>
- [18] Liang M, Borjigin T, Zhang Y, Liu B, Liu H, Guo H (2019) Controlled assemble of hollow heterostructured g-C<sub>3</sub>N<sub>4</sub>@CeO<sub>2</sub> with rich oxygen vacancies for enhanced photocatalytic CO<sub>2</sub> reduction. *Appl Catal B* 243:566–575
- [19] Liu C, Huang H, Ye L, Yu S, Tian N, Du X et al (2017) Intermediate-mediated strategy to horn-like hollow mesoporous ultrathin g-C<sub>3</sub>N<sub>4</sub> tube with spatial anisotropic charge separation for superior photocatalytic H<sub>2</sub> evolution. *Nano Energy* 41:738–748
- [20] Bajiri MA, Hezam A, Namratha K, Viswanath R, Drmash QA, Bhojya Naik HS et al (2019) CuO/ZnO/g-C<sub>3</sub>N<sub>4</sub> heterostructures as efficient visible light-driven photocatalysts. *J Environ Chem Eng* 7:103412. <https://doi.org/10.1016/j.jece.2019.103412>
- [21] Jiang D, Xiao P, Shao L, Li D, Chen M (2017) RGO-promoted all-solid-state g-C<sub>3</sub>N<sub>4</sub>/BiVO<sub>4</sub> Z-scheme heterostructure with enhanced photocatalytic activity toward the degradation of antibiotics. *Ind Eng Chem Res* 56:8823–8832
- [22] Shanmugam V, Sanjeevamuthu S, Jeyaperumal KS, Vairamuthu R (2019) Fabrication of heterostructured vanadium modified g-C<sub>3</sub>N<sub>4</sub>/TiO<sub>2</sub> hybrid photocatalyst for improved photocatalytic performance under visible light exposure and antibacterial activities. *J Indust Eng Chem* 76:318–332
- [23] Fajrina N, Tahir M (2019) Engineering approach in stimulating photocatalytic H<sub>2</sub> production in a slurry and monolithic photoreactor systems using Ag-bridged Z-scheme pCN/TiO<sub>2</sub> nanocomposite. *Chem Eng J* 374:1076–1095
- [24] Nie N, Zhang L, Fu J, Cheng B, Yu J (2018) Self-assembled hierarchical direct Z-scheme g-C<sub>3</sub>N<sub>4</sub>/ZnO microspheres with enhanced photocatalytic CO<sub>2</sub> reduction performance. *Appl Surf Sci* 441:12–22
- [25] Ohno T, Murakami N, Koyanagi T, Yang Y (2014) Photocatalytic reduction of CO<sub>2</sub> over a hybrid photocatalyst composed of WO<sub>3</sub> and graphitic carbon nitride (g-C<sub>3</sub>N<sub>4</sub>) under visible light. *J CO<sub>2</sub> Util* 6:17–25
- [26] Wang M, Shen M, Zhang L, Tian J, Jin X, Zhou Y et al (2017) 2D–2D MnO<sub>2</sub>/g-C<sub>3</sub>N<sub>4</sub> heterojunction photocatalyst: in-situ synthesis and enhanced CO<sub>2</sub> reduction activity. *Carbon* 120:23–31
- [27] Tonda S, Kumar S, Bhardwaj M, Yadav P, Ogale S (2018) g-C<sub>3</sub>N<sub>4</sub>/NiAl-LDH 2D/2D Hybrid heterojunction for high-performance photocatalytic reduction of CO<sub>2</sub> into renewable fuels. *ACS Appl Mater Interfaces* 10:2667–2678
- [28] Di T, Zhu B, Cheng B, Yu J, Xu J (2017) A direct Z-scheme g-C<sub>3</sub>N<sub>4</sub>/SnS<sub>2</sub> photocatalyst with superior visible-light CO<sub>2</sub> reduction performance. *J Catal* 352:532–541
- [29] Bafaqeer A, Tahir M, Amin NAS (2019) Well-designed ZnV<sub>2</sub>O<sub>6</sub>/g-C<sub>3</sub>N<sub>4</sub> 2D/2D nanosheets heterojunction with faster charges separation via pCN as mediator towards enhanced photocatalytic reduction of CO<sub>2</sub> to fuels. *Appl Catal B* 242:312–326
- [30] Xu D, Cheng B, Wang W, Jiang C, Yu J (2018) Ag<sub>2</sub>CrO<sub>4</sub>/g-C<sub>3</sub>N<sub>4</sub>/graphene oxide ternary nanocomposite Z-scheme photocatalyst with enhanced CO<sub>2</sub> reduction activity. *Appl Catal B* 231:368–380
- [31] Bao Y, Chen K (2018) Novel Z-scheme BiOBr/reduced graphene oxide/protonated g-C<sub>3</sub>N<sub>4</sub> photocatalyst: Synthesis, characterization, visible light photocatalytic activity and mechanism. *Appl Surf Sci* 437:51–61
- [32] Jo W-K, Kumar S, Eslava S, Tonda S (2018) Construction of Bi<sub>2</sub>WO<sub>6</sub>/RGO/g-C<sub>3</sub>N<sub>4</sub> 2D/2D/2D hybrid Z-scheme heterojunctions with large interfacial contact area for efficient charge separation and high-performance photoreduction of CO<sub>2</sub> and H<sub>2</sub>O into solar fuels. *Appl Catal B* 239:586–598

- [33] Xue W, Hu X, Liu E, Fan J (2018) Novel reduced graphene oxide-supported  $\text{Cd}_{0.5}\text{Zn}_{0.5}\text{S}/\text{g-C}_3\text{N}_4$  Z-scheme heterojunction photocatalyst for enhanced hydrogen evolution. *Appl Surf Sci* 447:783–794
- [34] Wang C, Wang G, Zhang X, Dong X, Ma C, Zhang X et al (2018) Construction of  $\text{g-C}_3\text{N}_4$  and  $\text{FeWO}_4$  Z-scheme photocatalyst: effect of contact ways on the photocatalytic performance. *RSC Advances* 8:18419–18426
- [35] Bafaqeer A, Tahir M, Amin NAS (2018) Synthesis of hierarchical  $\text{ZnV}_2\text{O}_6$  nanosheets with enhanced activity and stability for visible light driven  $\text{CO}_2$  reduction to solar fuels. *Appl Surf Sci* 435:953–962
- [36] Koci K, Obalova L, Solcova O (2010) Kinetic study of photocatalytic reduction of  $\text{CO}_2$  over  $\text{TiO}_2$ . *Chem Process Eng* 31:395–407
- [37] Davis ME, Davis RJ (2012) *Fundamentals of chemical reaction engineering*: Courier Corporation
- [38] Tan SS, Zou L, Hu E (2008) Kinetic modelling for photosynthesis of hydrogen and methane through catalytic reduction of carbon dioxide with water vapour. *Catal Today* 131:125–129
- [39] Yin Z, Qin J, Wang W, Cao M (2017) Rationally designed hollow precursor-derived  $\text{Zn}_3\text{V}_2\text{O}_8$  nanocages as a high-performance anode material for lithium-ion batteries. *Nano Energy* 31:367–376
- [40] Zhang T, Shen Y, Qiu Y, Liu Y, Xiong R, Shi J et al (2017) Facial synthesis and photoreaction mechanism of  $\text{BiFeO}_3/\text{Bi}_2\text{Fe}_4\text{O}_9$  heterojunction nanofibers. *ACS Sustain Chem Eng* 5:4630–4636
- [41] Lv H, Wu X, Liu Y, Cao Y, Ren H (2019) In situ synthesis of ternary  $\text{Zn}_{0.5}\text{Cd}_{0.5}\text{S}$  (0D)/RGO (2D)/ $\text{g-C}_3\text{N}_4$  (2D) heterostructures with efficient photocatalytic  $\text{H}_2$  generation activity. *Mater Lett* 236:690–693
- [42] Ong W-J, Tan L-L, Chai S-P, Yong S-T, Mohamed AR (2015) Surface charge modification via protonation of graphitic carbon nitride ( $\text{g-C}_3\text{N}_4$ ) for electrostatic self-assembly construction of 2D/2D reduced graphene oxide (rGO)/ $\text{g-C}_3\text{N}_4$  nanostructures toward enhanced photocatalytic reduction of carbon dioxide to methane. *Nano Energy* 13:757–770
- [43] Cao Y, Zhang Z, Long J, Liang J, Lin H, Lin H et al (2014) Vacuum heat-treatment of carbon nitride for enhancing photocatalytic hydrogen evolution. *J Mater Chem A* 2:17797–17807
- [44] Ma D, Wu J, Gao M, Xin Y, Ma T, Sun Y (2016) Fabrication of Z-scheme  $\text{g-C}_3\text{N}_4/\text{RGO}/\text{Bi}_2\text{WO}_6$  photocatalyst with enhanced visible-light photocatalytic activity. *Chem Eng J* 290:136–146
- [45] Shahid M, Liu J, Ali Z, Shakir I, Warsi MF (2013) Structural and electrochemical properties of single crystalline  $\text{MoV}_2\text{O}_8$  nanowires for energy storage devices. *J Power Sources* 230:277–281
- [46] Bai J, Li X, Liu G, Qian Y, Xiong S (2014) Unusual formation of  $\text{ZnCo}_2\text{O}_4$  3D Hierarchical twin microspheres as a high-rate and ultralong-life Lithium-Ion battery anode material. *Adv Funct Mater* 24:3012–3020
- [47] Xiang Q, Yu J, Jaroniec M (2011) Preparation and enhanced visible-light photocatalytic  $\text{H}_2$ -production activity of graphene/ $\text{C}_3\text{N}_4$  composites. *J Phys Chem C* 115:7355–7363
- [48] Lu X, Xu K, Chen P, Jia K, Liu S, Wu C (2014) Facile one step method realizing scalable production of  $\text{g-C}_3\text{N}_4$  nanosheets and study of their photocatalytic  $\text{H}_2$  evolution activity. *J Mater Chem A* 2:18924–18928
- [49] Hou Y, Wen Z, Cui S, Guo X, Chen J (2013) Constructing 2D porous graphitic  $\text{C}_3\text{N}_4$  nanosheets/nitrogen-doped graphene/layered  $\text{MoS}_2$  ternary nanojunction with enhanced photoelectrochemical activity. *Adv Mater* 25:6291–6297
- [50] Yuliati L, Itoh H, Yoshida H (2008) Photocatalytic conversion of methane and carbon dioxide over gallium oxide. *Chem Phys Lett* 452:178–182
- [51] László B, Baán K, Varga E, Oszkó A, Erdőhelyi A, Kónya Z et al (2016) Photo-induced reactions in the  $\text{CO}_2$ -methane system on titanate nanotubes modified with Au and Rh nanoparticles. *Appl Catal B* 199:473–484
- [52] Truc NTT, Hanh NT, Nguyen MV, Le Chi NTP, Van Noi N, Tran DT et al (2018) Novel direct Z-scheme  $\text{Cu}_2\text{V}_2\text{O}_7/\text{g-C}_3\text{N}_4$  for visible light photocatalytic conversion of  $\text{CO}_2$  into valuable fuels. *Appl Surf Sci* 457:968–974
- [53] Xiong X, Mao C, Yang Z, Zhang Q, Waterhouse GI, Gu L et al (2020) Photocatalytic  $\text{CO}_2$  reduction to CO over Ni single atoms supported on defect-rich zirconia. *Adv Energy Mater* 10:2002928
- [54] Han B, Wei W, Chang L, Cheng P, Hu YH (2016) Efficient visible light photocatalytic  $\text{CO}_2$  reforming of  $\text{CH}_4$ . *ACS Catal* 6:494–497
- [55] Hu X, Liu X, Tian J, Li Y, Cui H (2017) Towards full-spectrum (UV, visible, and near-infrared) photocatalysis: achieving an all-solid-state Z-scheme between  $\text{Ag}_2\text{O}$  and  $\text{TiO}_2$  using reduced graphene oxide as the electron mediator. *Catal Sci Technol* 7:4193–4205
- [56] Poznyak SK, Talapin DV, Kulak AI (2001) Structural, optical, and photoelectrochemical properties of nanocrystalline  $\text{TiO}_2\text{-In}_2\text{O}_3$  composite solids and films prepared by Sol–Gel method. *J Phys Chem B* 105:4816–4823
- [57] Chong S, Wang S, Tadé M, Ang HM, Pareek V (2011) Simulations of photodegradation of toluene and formaldehyde in a monolith reactor using computational fluid dynamics. *AIChE J* 57:724–734